

2

AD-A237 708



UNCLASSIFIED

ATION PAGE

Form Approved
OMB No. 0704-0188

to average 1 hour per response, including the time for reviewing instructions, searching existing data sources, writing the collection of information. Send comments regarding this burden estimate or any other aspect of this form, to Washington Headquarters Services, Directorate for Information Operations and Reports, 1215 Jefferson of Management and Budget, Paperwork Reduction Project (0704-0188), Washington, DC 20503.

DATE

3. REPORT TYPE AND DATES COVERED

April 19, 1991

Final, August 20, 1990 - Feb. 19, 1991

4. TITLE AND SUBTITLE

Compressive Stress-Induced Microcracks and Effective Elastic Properties of Limestone and Concrete

5. FUNDING NUMBERS

F49620-90-C-0060

6. AUTHOR(S)

Dr. Ziqiong Zheng
Dr. John D. McLennan
Mr. J. Wesley Martin

DTIC

7. PERFORMING ORGANIZATION NAME(S) AND ADDRESS(ES)

Terra Tek, Inc.
400 Wakara Way
Salt Lake City, Utah 84108

JUL 02 1991

8. PERFORMING ORGANIZATION REPORT NUMBER

TR 91-107

9. SPONSORING/MONITORING AGENCY NAME(S) AND ADDRESS(ES)

USAF, ~~AFOSR~~ AFOSR/NA
Air Force Office of Scientific Research
Bldg. 410
Bolling AFB, DC 20332-6448

10. SPONSORING/MONITORING AGENCY REPORT NUMBER

F49620-90-C-0060
61102F 3005/AF

11. SUPPLEMENTARY NOTES

12a. DISTRIBUTION/AVAILABILITY STATEMENT

Approved for public release;
distribution unlimited.

12b. DISTRIBUTION CODE

13. ABSTRACT (Maximum 200 words)

Stress-induced microstructural alterations were observed in Indiana limestone and one type of using low wetting concrete, point metal alloy injection technique. Average microcrack length and aperture decreased with an increase in applied confining stress. Microcrack density increased with an increase in confining stress. Most microcracks were oriented at a small angle to the maximum compression direction. Theoretical solutions for effective moduli and Poisson's ratios of an axisymmetrically microfractured material were obtained using energy conservation principles. Results showed that all effective moduli are less than for the original undamaged and decreased with an increase in microcrack density. Ultrasonic velocities measured concurrently during static compression tests conformed the observations. "Dynamic" stress-strain curves constructed from the measured ultrasonic velocities showed relatively similar behavior as the static stress-strain curves. Both static and dynamic moduli decreased with an increase in axial deviatoric stress. This provides a possibility in future research to extrapolate microcrack density at any given stress state from one observed density by combining convenient ultrasonic measurement and theoretical solutions obtained from this research.

14. SUBJECT TERMS

Microcrack, Damage, Concurrent Measurements, Effective Property, Heterogeneity, Microstructural Alteration, Alloy Injection, Preservation, "Dynamic" Stress-Strain Curve.

15. NUMBER OF PAGES

59

16. PRICE CODE

17. SECURITY CLASSIFICATION OF REPORT

Unclassified

18. SECURITY CLASSIFICATION OF THIS PAGE

Unclassified

19. SECURITY CLASSIFICATION OF ABSTRACT

Unclassified

20. LIMITATION OF ABSTRACT

PHASE I FINAL TECHNICAL REPORT

Compressive Stress-Induced Microcracks and Effective
Elastic Properties of Limestone and Concrete
Phase I Top Number AF90-186



Submitted to:

AFOSR/XOT

Building 410, Room A-119
Bolling AFB, D.C. 20332-6448

Attn: Dr. Spencer Wu

Accession For	
DTIC GRAAL	<input checked="" type="checkbox"/>
DTIC Tab	<input type="checkbox"/>
Unprocessed	<input type="checkbox"/>
Justification	
by	
Distribution/	
Availability Codes	
Dist	Avail and/or Special
A-1	

TR91-107
April 1991

TerraTek

TerraTek Inc.

91-03886



PHASE I FINAL TECHNICAL REPORT

**Compressive Stress-Induced Microcracks and Effective
Elastic Properties of Limestone and Concrete
Phase I Top Number AF90-186**

Prepared by:

**Z. Zheng
J. McLennan
W. Martin**

Submitted to:

**AFOSR/XOT
Building 410, Room A-119
Bolling AFB, D.C. 20332-6448**

Attn: Dr. Spencer Wu

Submitted by:

**TERRA TEK, INC.
420 Wakara Way
Salt Lake City, Utah 84108**

**TR91-107
April 1991**

FORWARD

The effort discussed in this report was performed by Terra Tek, Inc., 420 Wakara Way, Salt Lake City, Utah 84108, sponsored by the Air Force Office of Scientific Research (AFSC), under Contract F49620-90-C-0060. The effort was conducted under the management of Dr. Spencer Wu acting as Technical Manager for Air Force Office of Scientific Research. The United States Government is authorized to reproduce and distributes reprints for governmental purposes notwithstanding and copyright notation hereon.

EXECUTIVE SUMMARY

Detailed microstructural alterations (damage) in Indiana limestone and one type of concrete under different loading conditions have been observed using liquid metal alloy preservation techniques. The technique of using low melting point alloy is proved to be effective, convenient and reliable. The basic observations show the following:

The basic mechanism for initiation of extensile microcracks in a material under compression are the localized tensile stresses induced by heterogeneities. These localized tensile stresses include bending of long grains, Herzian contact tension between adjacent grains, mismatching elastic properties, boundary discontinuities and pore space and soft inclusion induced tension. Once the microcracks are generated, regardless of the initial orientation, they generally propagate in the direction of the maximum compression. The propagation of microcracks is controlled by the combination of local tensile stress and the overall confining stress, before any interaction takes place. It is hypothesized that the generation and propagation of microcracks also change the local stress distribution, which in turn affects the generation of other microcracks. Preliminary statistical results for both the concrete and limestone show that the average length of the microcracks decreases with an increase in confining stress. Average aperture of the microcracks also decreases with an increase in confining stress. The aspect ratio (the ratio between the aperture of a crack and its length) remains relatively constant for concrete and fluctuates for Indiana limestone. Most of the microcracks are parallel or subparallel to the direction of the maximum compressive stress. The average orientations of microcracks in all of the samples tested are within 15 degrees of the maximum compressive direction. The density of microcracks (the number of microcracks per unit observed area) increases with an increase in confining stress. The relationship between microcrack distribution and applied stresses could not be quantified in this phase of the research. The macroscopic failure of Indiana limestone samples under unconfined conditions is usually in axial splitting, and under high confining pressure in the form of shear bands. The axial splitting of specimens is usually the result of one or several extensile cracks propagating all the way to the ends of the samples. The shear bands are observed to be formed from many short extensile microcracks which are subparallel to the direction of the maximum compression and with their centers slightly offset from each other.

Ultrasonic wave velocities were measured concurrently during static compression tests. Artificial "dynamic" stress-strain curves were reconstructed from the dynamic modulus calculated from the velocities. "Dynamic" stress-strain curves reconstructed from ultrasonic velocities showed similar behavior to the concurrently generated static stress-strain curves. Both static and dynamic moduli decreased near peak stress (strength) level, indicating the generation and interaction of microcracks (damage). This suggests that if a relationship between the "dynamic" and static stress-strain curves can be established, a non-destructive method such as ultrasonic detection can be used to quantitatively determine and detect the static behavior of a geomaterial and the damage level.

Using energy conservation principles, theoretical derivations of effective elastic properties of an isotropic material containing axisymmetrically distributed microcracks, showed that moduli of a material decrease with an increase in damage density. This is verified by independent concurrent triaxial compression tests, ultrasonic velocity measurements and microstructural observations. These results show that if a one-to-one relationship can be established between the theoretically derived formulations and microcrack distribution, it could be possible to extrapolate microcrack density at any stage of loading. This requires a calibration of the theoretical formulations given the stress conditions and quantification of microcrack distribution under the same conditions. In a Phase II proposal for this research, submitted under separate cover, this calibration and microcrack density extrapolation is proposed.

TABLE OF CONTENTS

1	ADMINISTRATIVE BACKGROUND:	1
2	TECHNICAL BACKGROUND:	1
2.1	Issues to be Addressed	1
2.2	TASK 1: Experimentation, Microstructural Observation and Statistical Analysis	2
2.3	Task 2: Theoretical Study of Effective Elastic Properties as Functions of Microfractures	3
3	INTRODUCTION	4
4	EXPERIMENTAL TECHNIQUE	5
5	RESULTS	7
5.1	"Static" Stress-Strain Curves	7
5.2	"Dynamic" Stress-Strain Curves	7
5.3	Comparison of Static and Reconstructed Dynamic Stress-Strain Curves	13
5.4	Photomicrograph	13
5.5	Microcrack Observations	14
5.6	"Dynamic" Stress-Strain Curves	25
6	THEORETICAL CONSIDERATIONS ON MECHANICAL PROPERTY-MICROCRACK RELATIONSHIP	27
6.1	Background	27
6.2	Constitutive Equations	27
6.3	Equilibrium Equations	29
6.4	Elastic Wave Motion Equations	31
6.5	Elastic Relations for an Axisymmetrically Microcracked Material	32
6.6	Elastic Constraint (Energy Conservation) for an Isotropic Material with an Anisotropic Extensile Microcrack Distribution	33
6.7	Strain Energy for a Penny-Shaped Crack	35
6.8	Elastic (P and S) Wave Propagation	36
6.8.1	P-Wave Propagating in Direction 1	36
6.8.2	Shear (S) Wave Traveling in Direction 1: (Particle Motion in a Plane with its Normal Parallel to Direction 1)	38
6.8.3	P and S Wave Traveling Orthogonal to Direction 1	38
7	CONCLUSIONS AND OBSERVATIONS	42
8	ACKNOWLEDGEMENTS	44

9	REFERENCE	44
---	-----------------	----

LIST OF FIGURES

Figure 1. Complete stress-strain curve showing different stages of rock behavior.	4
Figure 2. Strain-gaged cantilevers for strain measurements.	6
Figure 3. Quasi-static stress-strain plot for an Indiana limestone sample, oriented vertically and subjected to zero confining stress. The periodic levels of constant stress difference indicate where dynamic measurements were performed.	8
Figure 4. Quasi-static stress-strain plot for an Indiana limestone sample, oriented vertically and subjected to a confining stress of 2500 psi. The periodic levels of constant stress difference indicate where dynamic measurements were performed.	9
Figure 5. Quasi-static stress-strain plot for an Indiana limestone sample, oriented vertically and subjected to a confining stress of 5000 psi. The periodic levels of constant stress difference indicate where dynamic measurements were performed.	9
Figure 6. Quasi-static stress-strain plot for a concrete sample, subjected to zero confining stress. The periodic levels of constant stress difference indicate where dynamic measurements were performed.	10
Figure 7. Quasi-static stress-strain plot for a concrete sample, subjected to a confining stress of 5000 psi. The periodic levels of constant stress difference indicate where dynamic measurements were performed.	10
Figure 8. "Dynamic" stress-strain curve plot for an Indiana limestone sample, oriented vertically and subjected to zero confining stress. The plot was constructed from dynamic modulus calculated from the ultrasonic wave velocities.	11
Figure 9. "Dynamic" stress-strain curve plot for an Indiana limestone sample, oriented vertically and subjected to a confining stress of 2500 psi. The plot was constructed from dynamic modulus calculated from the ultrasonic wave velocities.	11
Figure 10. "Dynamic" stress-strain curve plot for an Indiana limestone sample, oriented vertically and subjected to a confining stress of 5000 psi. The plot was constructed from dynamic modulus calculated from the ultrasonic wave velocities.	12
Figure 11. "Dynamic" stress-strain curve plot for a concrete sample, oriented vertically and subjected to a zero confining stress. The plot was constructed from dynamic modulus calculated from the ultrasonic wave velocities.	12
Figure 12. "Dynamic" stress-strain curve plot for a concrete sample, oriented vertically and subjected to a confining stress of 5000 psi. The plot was constructed from dynamic modulus calculated from the ultrasonic wave velocities.	13
Figure 13a. Photomicrograph of an axial cross section Indiana limestone sample, subjected to a zero confining stress (post-peak). The width of the photomicrograph is the diameter of the sample and is one inch in dimension.	15

Figure 13b. Trace of dominant microcracks shown on the photomicrograph in Figure 13a.	16
Figure 14a. Photomicrograph of an axial cross section Indiana limestone sample, subjected to a confining stress of 2500 psi (post-peak). The width of the photomicrograph is the diameter of the sample and is one inch in dimension.	17
Figure 14b. Trace of dominant microcracks shown on the photomicrograph in Figure 14a.	18
Figure 15a. Photomicrograph of an axial cross section Indiana limestone sample, subjected to a confining stress of 5000 psi (post-peak). The width of the photomicrograph is the diameter of the sample and is one inch in dimension.	19
Figure 15b. Trace of dominant microcracks shown on the photomicrograph in Figure 15a.	20
Figure 16a. Photomicrograph of an axial cross section of concrete sample, subjected to a zero confining stress (post-peak). The width of the photomicrograph is the diameter of the sample and is one inch in dimension.	21
Figure 16b. Trace of dominant microcracks shown on the photomicrograph in Figure 16a.	22
Figure 17a. Photomicrograph of an axial cross section of concrete sample, subjected to a confining stress of 5000 psi (post-peak). The width of the photomicrograph is the diameter of the sample and is one inch in dimension.	23
Figure 17b. Trace of dominant microcracks shown on the photomicrograph in Figure 17a.	24
Figure 18. Schematic representation of the principles of superposition applied to a material containing microcracks.	34
Figure 19. Penny-shaped crack in an infinite body under uniform tension and shear.	35
Figure 20. Stresses acting on a penny-shaped crack whose normal is orthogonal to direction 1 and at an angle ϕ to direction 2.	40

1 Administrative Background:

The following reports on a Phase I SBIR, awarded to Terra Tek, Inc. The specifics are:

Topic Number: AF 90-186

Title: Statistical Study of Stress-Induced Microstructures in Selected Rock and Concrete

Submitted by: Terra Tek, Inc.
420 Wakara Way
Salt Lake City, Utah 84108

Submitted to: AFOSR/XOT
Building 410, Rm A-119
Bolling AFB, DC 20332-6448

2 Technical Background:

An abbreviated summary of the work performed is as follows:

2.1 Issues to be Addressed

In this proposed study, the following questions will be addressed:

- What are the mechanisms for the generation of stress induced microcracks in granular and porous brittle material such as limestone, sandstone and concrete, when these materials are subjected to overall compression? What are the effects of inherent/pre-existing microstructures in these porous material on the generation of microcracks under loading?
- What are the major factors controlling the propagation of fractures once they are initiated? Are they related to the microstructures or stress conditions or both? Can these effects be quantified?
- What are the interactions between microcracks? How do local stress concentrations around the cracks affect the generation and propagation of other cracks?
- What is the relationship between microcrack density, length and aperture and stress conditions?

- What are the mechanisms of macroscopic failure (axial splitting, shear faulting and drumming out) in test specimens? How do microcracks interact to cause these macroscopic failures?
- How is the dilation (expansion in the minimum stress directions) of specimens related to the generation and propagation of microcracks? What role does pore collapse play?
- What are the effective elastic moduli when microcracks are generated, especially the anisotropic elastic moduli in relation to the microcrack density, length and aperture? What are the anisotropic Poisson's ratios?

2.2 TASK 1: Experimentation, Microstructural Observation and Statistical Analysis

Objective: To statistically study and quantify the generation, propagation and interaction between microstructures generated under different stress conditions and the mechanisms of generation of these stress-induced microstructures.

Technical Approach: Experiments were performed on one type of rock and one type of concrete. Specimens were subjected to uniaxial and triaxial compression, and tension. The microstructures before and after the tests were examined using electron microscopy.

- Rock and concrete specimens, one inch in diameter and two inches long, were endground flat and parallel to a tolerance of ± 0.001 inch.
- A section of each specimen was preserved for microscopic observation. These virgin specimens were used as a reference for comparison with post-test specimens.
- The specimens were carefully weighed and dimensions recorded. Each specimen was instrumented with strain-gauged cantilevers for strain measurements.
- Each specimen was installed into a servo-controlled stiff testing machine. Strain rates for the tests were low (10^{-6} in/in/sec to 5×10^{-6} in/in/sec) to assure pseudo-static conditions. With strain control, the complete stress-strain curve (including the post-failure region) was readily reordered.
- At the stress or strain of interest (linear elastic deformation region, microcrack generation region, or, post-failure region on a stress-strain curve), the test was stopped and specimens were unloaded. Unloading was done slowly to avoid introducing additional microcracks.
- To preserve the microstructure of the specimens, petrographic epoxy or low melting point metal was injected. The low melting point metal injection technique has been used very successfully for preserving microstructures (Zheng et al. 1989 and Zheng, 1989).

With a surface tension of 400 mN/m, low melting point metal such as Wood's metal (melting point at 89°C) will penetrate cracks with apertures of 0.08 micrometer, as a liquid under a pore pressure of 10 MPa.

- These specimens were sectioned parallel and perpendicular to their axes. Sections for microscopic observation using scanning electron microscopy and petrographic microscopy (thin sections) were prepared.

- From the microscopic observations, the characteristics of stress-induced microstructures in the specimens will be recorded. This will include the density, length distribution, aperture distribution and orientation of the microcracks and fractures.

- These characteristics of the stress-induced microstructures were statistically analyzed in association with the stress conditions to which the specimen was subjected.

- Results of the statistical analysis of such stress-microstructure relations provided the basis for the effective elastic property analysis in the theoretical portion of this proposal (Task 2).

Output: Statistical representation of the distribution of microcracks generated under different stress conditions. These include the density, orientation, aperture and length distribution of microcracks, as functions of stress conditions.

2.3 Task 2: Theoretical Study of Effective Elastic Properties as Functions of Microfractures

Objective: In this task, the anisotropic effective elastic properties due to stress induced microstructures was analytically derived.

Technical Approach: The basis of this theoretical study is the principle of energy conservation. The elastic strain energy derived using effective mechanical properties should balance the elastic strain energy used in deformation of the intact portion of a fractured material and the fracture energy in opening or closing of the fractures:

The derived anisotropic elastic properties were validated qualitatively using the experimental results (stress-strain curves and statistical distribution of microstructures induced by different stress conditions) from Task 1 and artificial material by the means of non-destructive (acoustic) elastic property measurements.

Output: Anisotropic effective elastic properties as functions of microcrack distributions (density, orientation, length and aperture), summary of theoretical considerations in interrelating micro- and macro- characteristics.

3 Introduction

Mechanical properties of a material change when applied stresses become high enough to induce microstructural alterations. This is specially true for geomaterials, which are generally heterogeneous and are often brittle. Interaction between these microstructural alterations can ultimately cause macroscopic failure of the materials. During the occurrence of these microstructural alterations (damage), the macroscopic mechanical behavior of a material may also change. Such evolution is usually represented as changes in the elastic modulus of the material. To appreciate this, consider Figure 1. This is a "typical" axial deviatoric stress-strain curve generated during triaxial compression. The curve shows four generic portions or segments. In segment A, initial large deformation due to the closure of microcracks and pores is characteristic. The slope of the stress-strain curve (elastic modulus) increases with increases in the axial stress as compaction of the material proceeds, reaching a constant value. The slope in this linear portion (segment B) is usually taken as the elastic modulus of the material. With further elevation of the deviatoric stress (segment C), an alternate trend begins, usually at $\approx 70\%$ to 80% of the peak stress level. In this regime, the stress-strain curve manifests a decreasing slope due to the generation and propagation of microcracks, pore collapse and other irreversible microstructural changes. In segment D, generally regarded as the post-failure or strain softening regime, deformation increases with decreasing axial stress. In post-peak regimes characteristic phenomena are due to the interaction of microcracks and large scale microstructural alterations. An understanding of the relationship between the microstructural alterations and the macroscopic behavior of a material is important in understanding mechanisms of geomaterial failure.

The behavior of rocks under compressive stresses has been studied by vast numbers of researchers. For example, Wawersik and Fairhurst (1971) studied the macroscopic behavior of different types of rocks in the post-failure region. Hallbauer et al. (1973) studied microdamage density in rocks along a stress-strain curve and showed that the density of microcracks increases as the applied stress increases. Fonseka et al. (1985) studied microcrack development under compressive stress using scanning electron microscopy and acoustic emission. Zheng et al. (1989) studied microcrack distribution as a function of confining stress conditions using low melting point alloy injection techniques. Most of these studies were performed on rock. The measurements and observations required destruction of the material (except for the technique used by Fonseka et al. 1985), and the information obtained is only applicable to the stress state under which the material

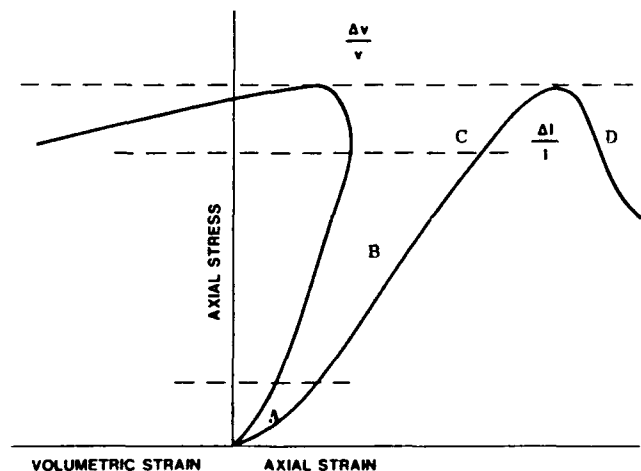


Figure 1. Complete stress-strain curve showing different stages of rock behavior.

microstructure was preserved. The research presented here was initiated to observe and record damage of Indiana limestone and concrete (with small aggregate) at different stages of triaxial compression. Methods used included concurrent measurement of static (stress and strain measurements) and dynamic (ultrasonic velocity measurements) properties and injection of a low melting point metal alloy.

4 Experimental Technique

Cylindrical Indiana limestone (composition¹: calcium carbonate = 97.39%, magnisium carbonate = 1.2%, silica = 0.69%, alumina 0.44%, iron oxide 0.18% and porosity \approx 10%) and small aggregate concrete specimens, one inch in diameter by nominally two inches long, were endground parallel to within a tolerance of ± 0.001 inch. These specimens were then oven dried at 110 °C for at least 48 hours. Before testing , each specimen was placed between two stainless steel endcaps and jacketed with a Teflon sleeve, to prevent intrusion of confining fluid into the specimens. Each of the endcaps was contained embedded ultrasonic transducers as well as a central axial hole and grooves on the faces contacting the specimen for pore fluid access. Each specimen was then instrumented with strain measurement devices (strain-gaged cantilevers, as shown in Figure 2) and placed in a pressure vessel.

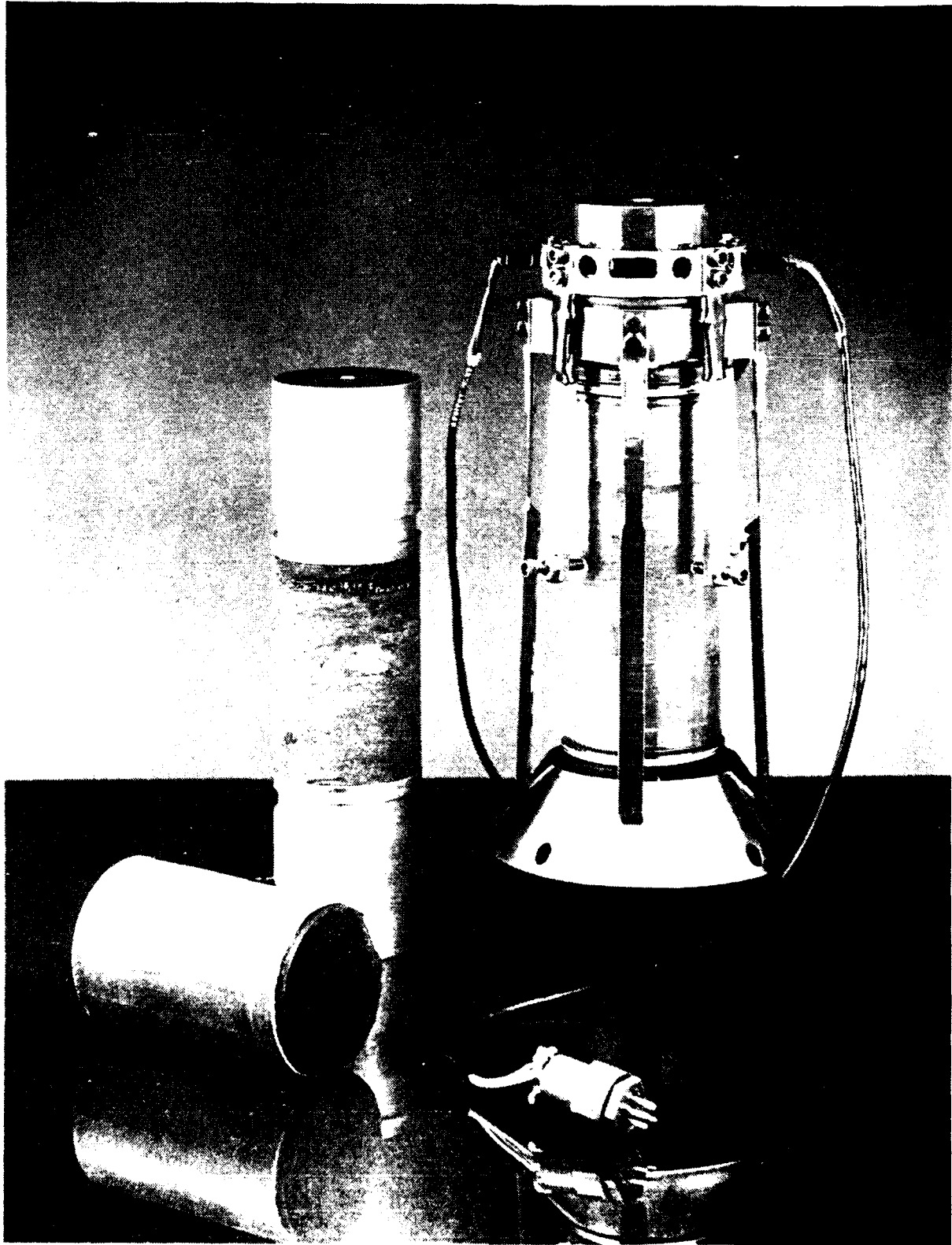
To preserve microstructure and microstructural alterations evolving during a test, a low melting point metal alloy, Cerrosafe[®], was used as the pore fluid. Cerrosafe[®] is composed of 42.5% Bi, 37.7% Pb, 11.3% Sn and 8.5% Cd, with a melting point of 87 °C². It has been previously used for porosimetry studies (Yadev et al., 1984), fracture contact area studies (Pyrak et al., 1987) and microstructure preservation (Zheng et al, 1987, Ewy et al., 1989, Zheng et al, 1989, Suarez et al, 1990). By injecting liquid alloy into a specimen and allowing it to solidify in place, the microstructure existing at the instant of alloy solidification is preserved. The technique not only preserves microstructure under applied stress or strain boundary conditions, but also provides a means of distinguishing these discontinuities from those generated during unloading and subsequent material handling. With a surface tension of 400 mN/cm², the alloy can penetrate fractures with apertures of as little as 0.08 mm, with an injection (pore) pressure of 10 MPa (1450 psi).

Before testing, the temperature of the vessel was elevated to 92°C. A hydrostatic stress of 2000 psi was applied to the specimen. Next, pore pressure was elevated to 1500 psi. An equilibrium period was imposed to insure that the alloy penetrated every accessible void in the specimen. The confining pressure was then increased to the required level for testing. Next, a deviatoric (axial) stress was increased. This axial deviatoric stress was increased under strain (axial) control, at a rate of 10⁻⁵ in/in/sec.

¹ Handbook, Indiana Limestone Institute of America, Inc., 17th edition, 1986.

² Cerro Alloys Application Data, Cerro Metal Products Co.

Figure 2. Strain-gaged cantilevers for strain measurements.



In order to examine elastic property change as a function of microstructural evolution "continuously" on the same sample, concurrent ultrasonic velocity measurements were performed. Microscopic observations only allow assessment of the state of material at the moment of preservation. The endcaps used during measurements contained embedded longitudinal (P) wave and shear (S) wave transducers for emission and receiving of ultrasonic impulses. As testing proceeded, the velocities of these P and S waves were periodically measured. Dynamic Young's modulus and Poisson's ratio were calculated from the velocities and stress-strain curves were artificially reconstructed from these calculated elastic (dynamic) properties. The stress-strain curves were later compared with those generated from direct measurement of stress and strain.

The alloy impregnated specimens were sectioned parallel to their axes and surface polished for microscopic observation and statistical studies. Microcrack density, average orientation, length and aperture were recorded in the same manner as described by Zheng et al; (1989). The statistical results were then used in effective property measurements and evaluation.

5 RESULTS

5.1 "Static" Stress-Strain Curves

Figures 3 to 7 are typical stress-strain curves for samples tested under different confining stress conditions. Figures 3, 4 and 5 show the stress-strain behavior of Indiana limestone under confining stresses of 0, 2500 and 5000 psi, respectively. Figures 6 and 7 show the stress-strain behavior of concrete specimens subjected to confining stresses of 0 and 5000 psi.

5.2 "Dynamic" Stress-Strain Curves

Figures 8 to 12 are analogous stress-strain curves artificially constructed from moduli determined from the concurrent ultrasonic measurements. These figures correspond directly with Figures 3 through 7, performed at a quasi-static strain rate. Detailed data is provided in Appendix A. The "dynamic" stress-strain curves were constructed by using dynamic modulus as the secant modulus of a stress-strain curve at corresponding stress levels³. The dynamic modulus and Poisson's ratio were calculated using the following equations (Jaeger and Cook, 1976):

³ Damage mechanics considerations frequently adopt secant modulus because of the inconsistency of tangential moduli in post peak regions (negative).

$$E_D = \rho V_s^2 \frac{3V_p^2 - 4V_s^2}{V_p^2 - V_s^2}$$

and

$$\nu_D = \frac{1}{2} \frac{V_p^2 - 2V_s^2}{V_p^2 - V_s^2}$$

where:

E_D = Dynamic Young's modulus

ν_D = Dynamic Poisson's ratio

ρ = Material density

V_p = P-Wave velocity

V_s = S-Wave velocity

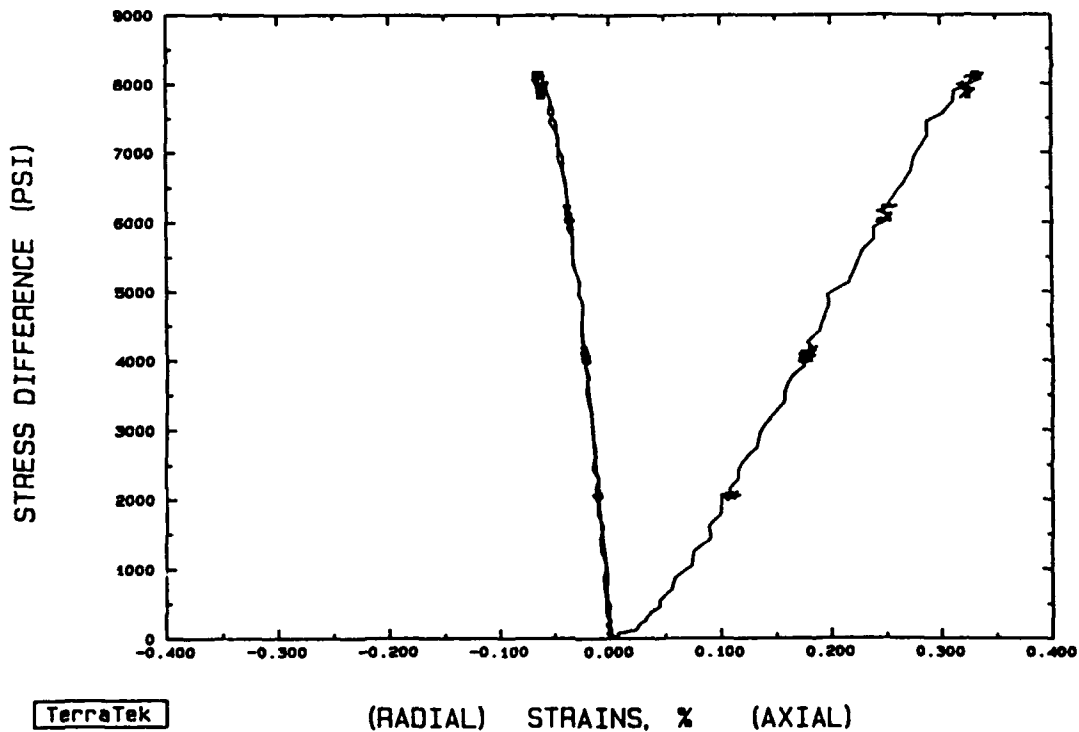


Figure 3. Quasi-static stress-strain plot for an Indiana limestone sample, oriented vertically and subjected to zero confining stress. The periodic levels of constant stress difference indicate where dynamic measurements were performed.

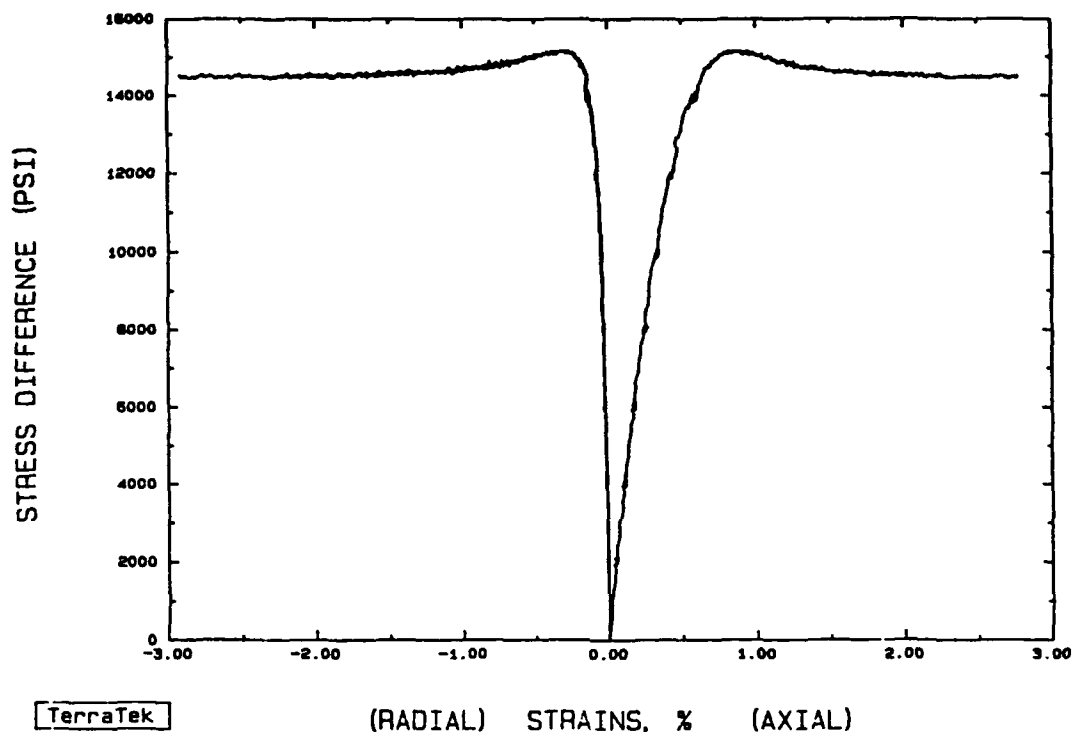


Figure 4. Quasi-static stress-strain plot for an Indiana limestone sample, oriented vertically and subjected to a confining stress of 2500 psi. The periodic levels of constant stress difference indicate where dynamic measurements were performed.

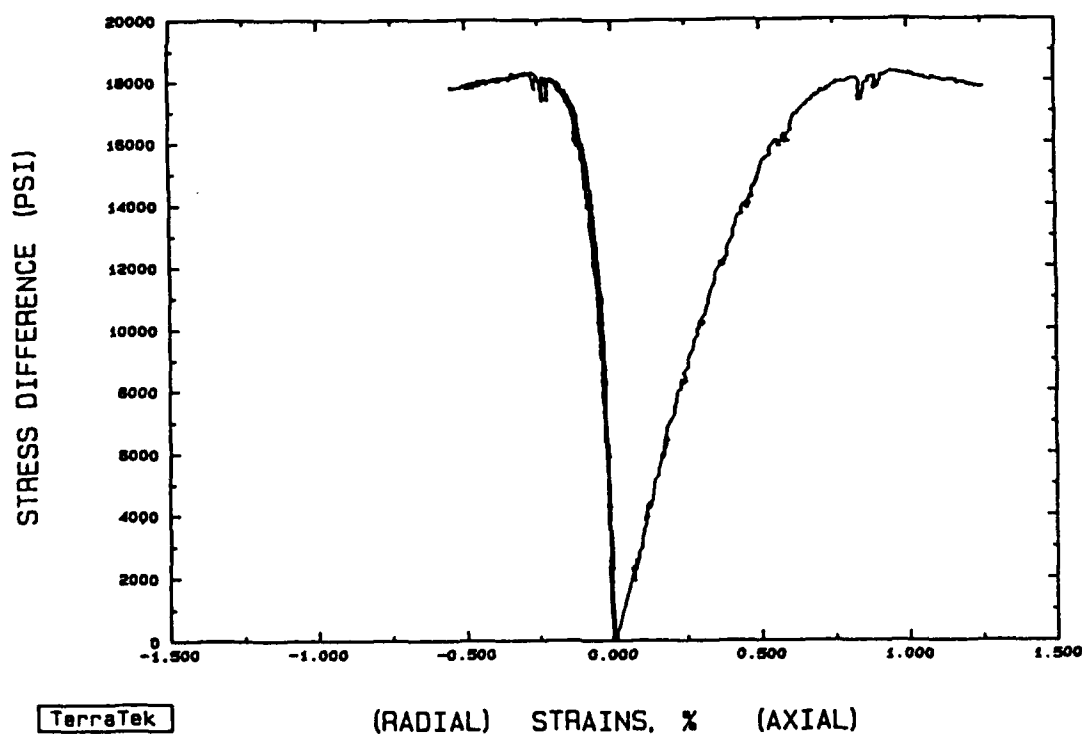


Figure 5. Quasi-static stress-strain plot for an Indiana limestone sample, oriented vertically and subjected to a confining stress of 5000 psi. The periodic levels of constant stress difference indicate where dynamic measurements were performed.

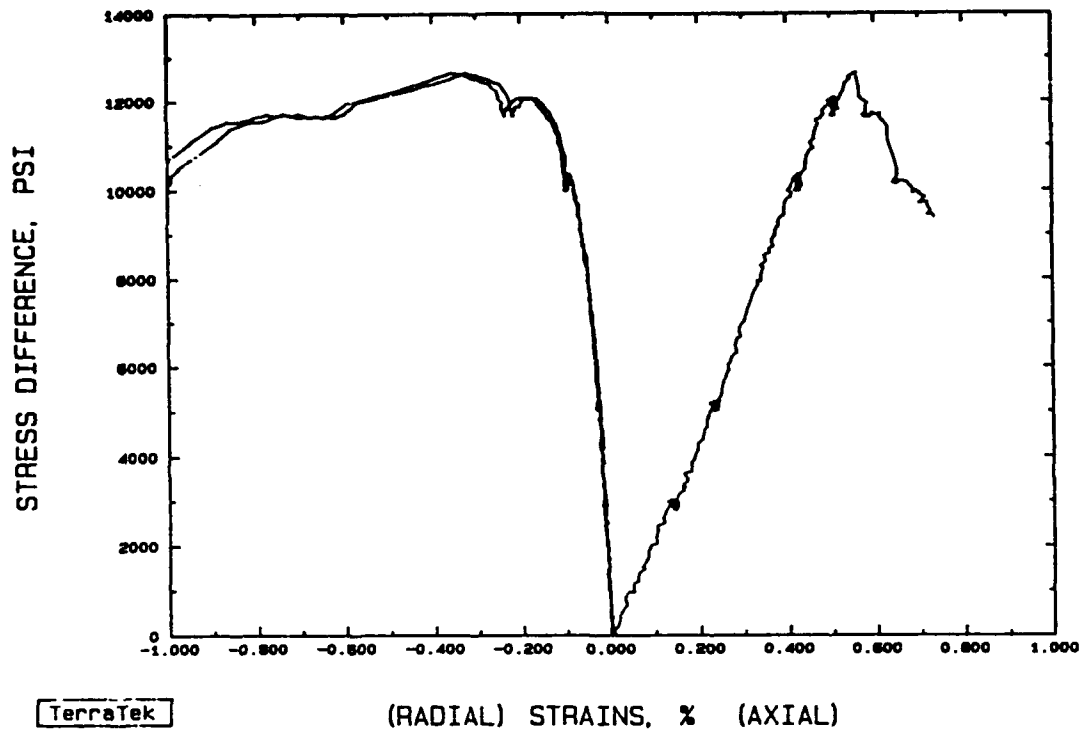


Figure 6. Quasi-static stress-strain plot for a concrete sample, subjected to zero confining stress. The periodic levels of constant stress difference indicate where dynamic measurements were performed.

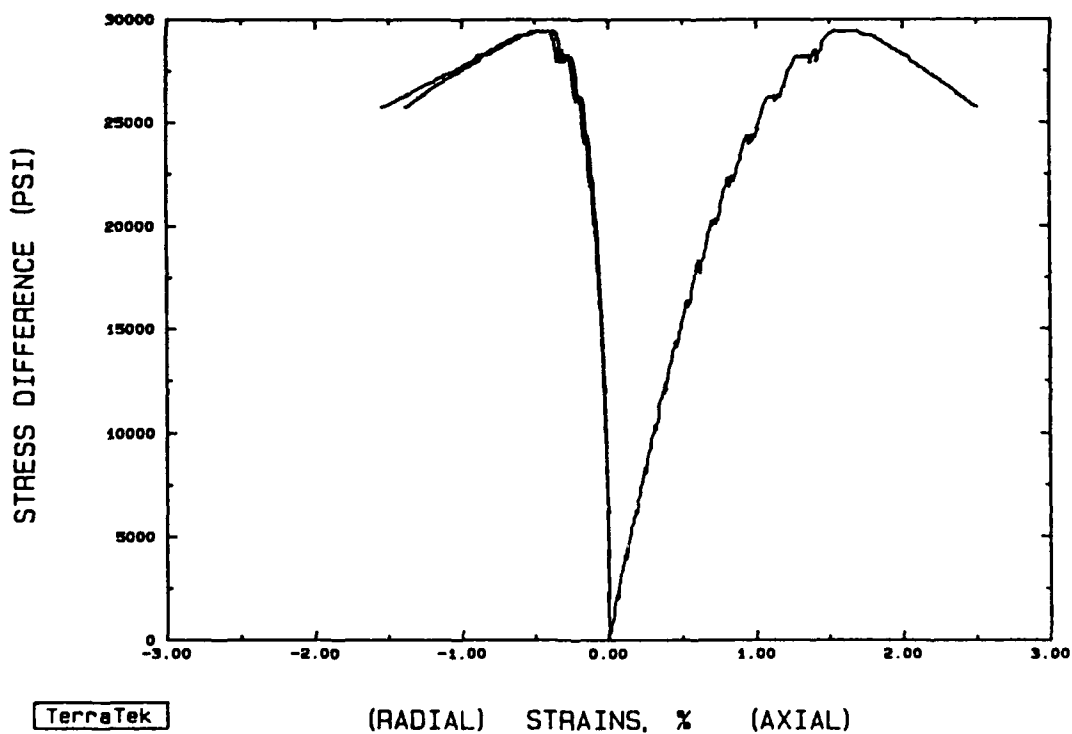


Figure 7. Quasi-static stress-strain plot for a concrete sample, subjected to a confining stress of 5000 psi. The periodic levels of constant stress difference indicate where dynamic measurements were performed.

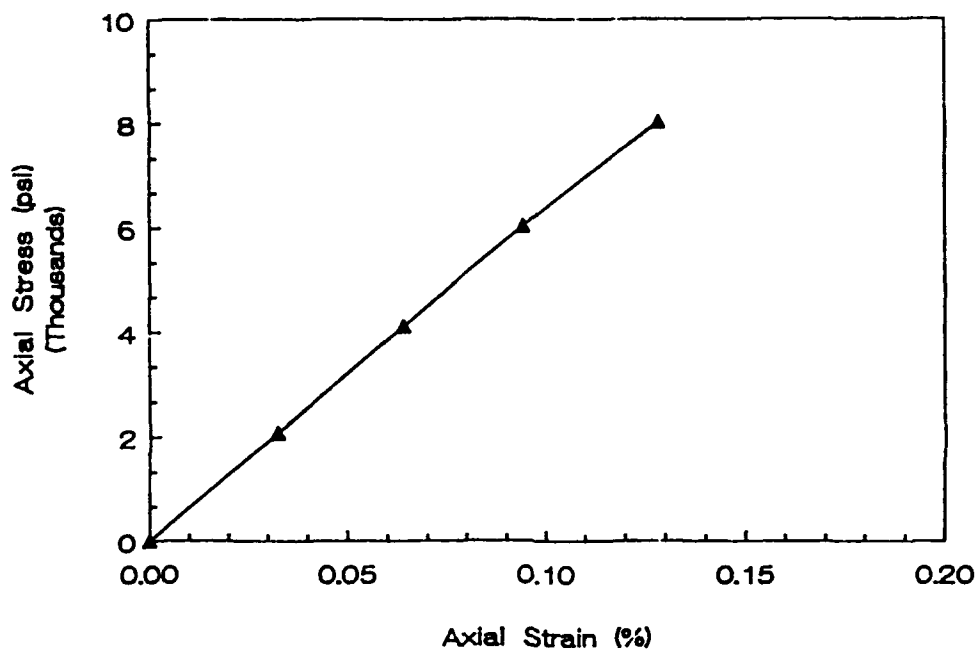


Figure 8. "Dynamic" stress-strain curve plot for an Indiana limestone sample, oriented vertically and subjected to zero confining stress. The plot was constructed from dynamic modulus calculated from the ultrasonic wave velocities.

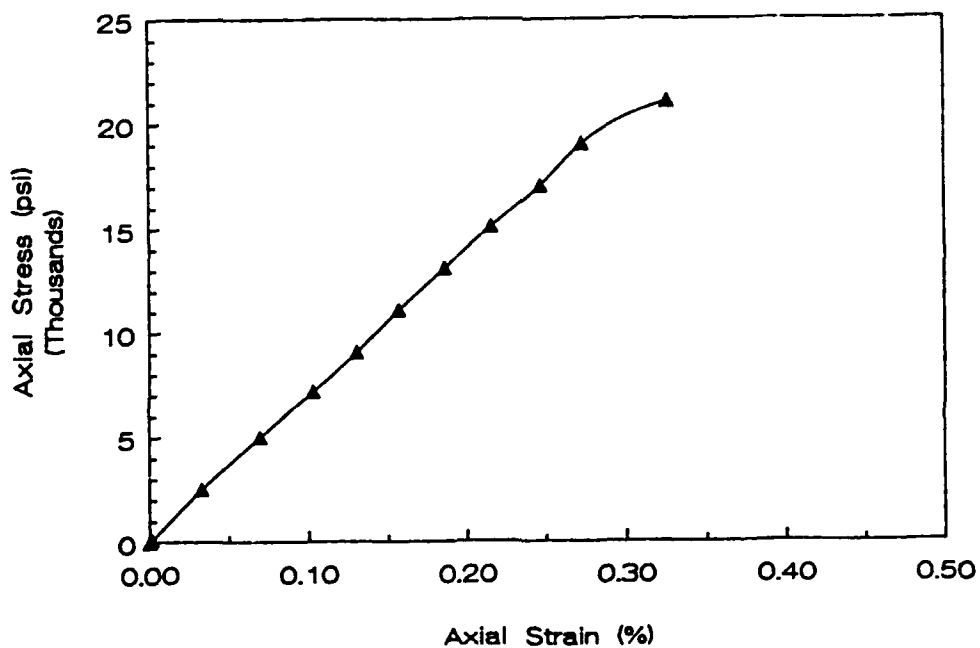


Figure 9. "Dynamic" stress-strain curve plot for an Indiana limestone sample, oriented vertically and subjected to a confining stress of 2500 psi. The plot was constructed from dynamic modulus calculated from the ultrasonic wave velocities.

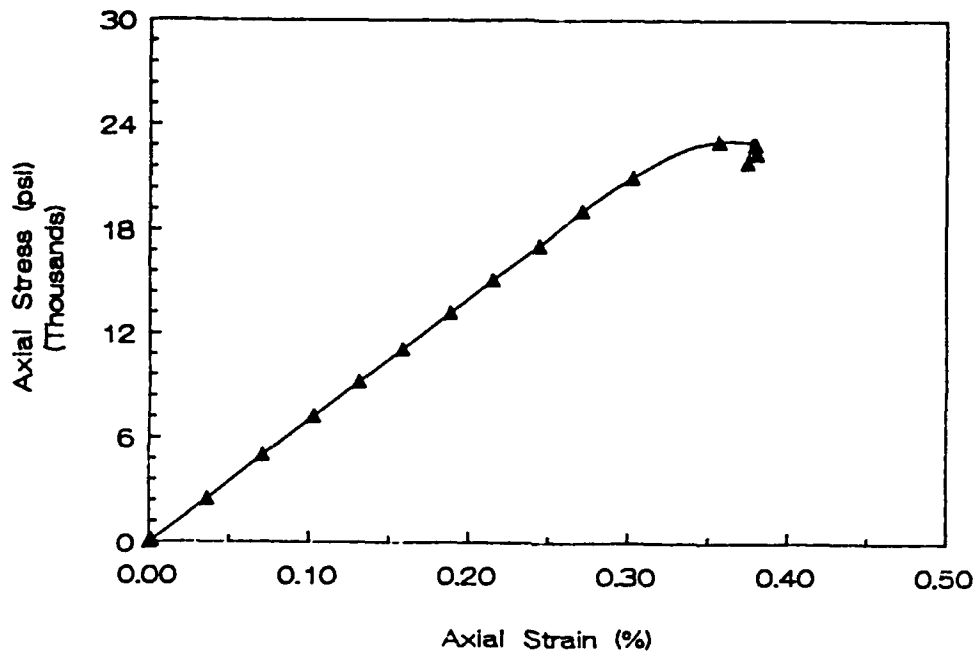


Figure 10. "Dynamic" stress-strain curve plot for an Indiana limestone sample, oriented vertically and subjected to a confining stress of 5000 psi. The plot was constructed from dynamic modulus calculated from the ultrasonic wave velocities.

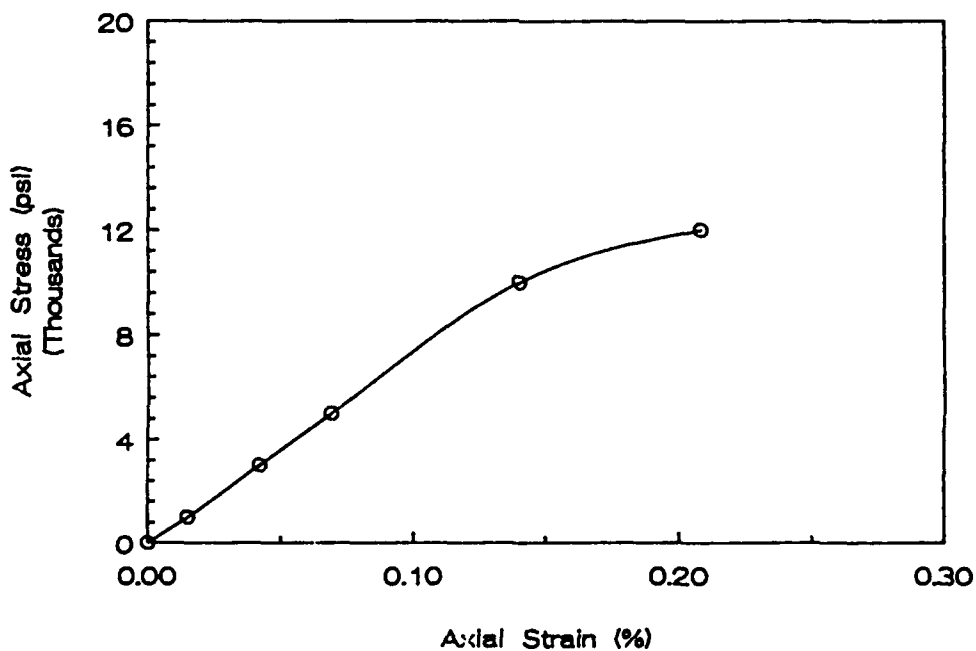


Figure 11. "Dynamic" stress-strain curve plot for a concrete sample, oriented vertically and subjected to a zero confining stress. The plot was constructed from dynamic modulus calculated from the ultrasonic wave velocities.

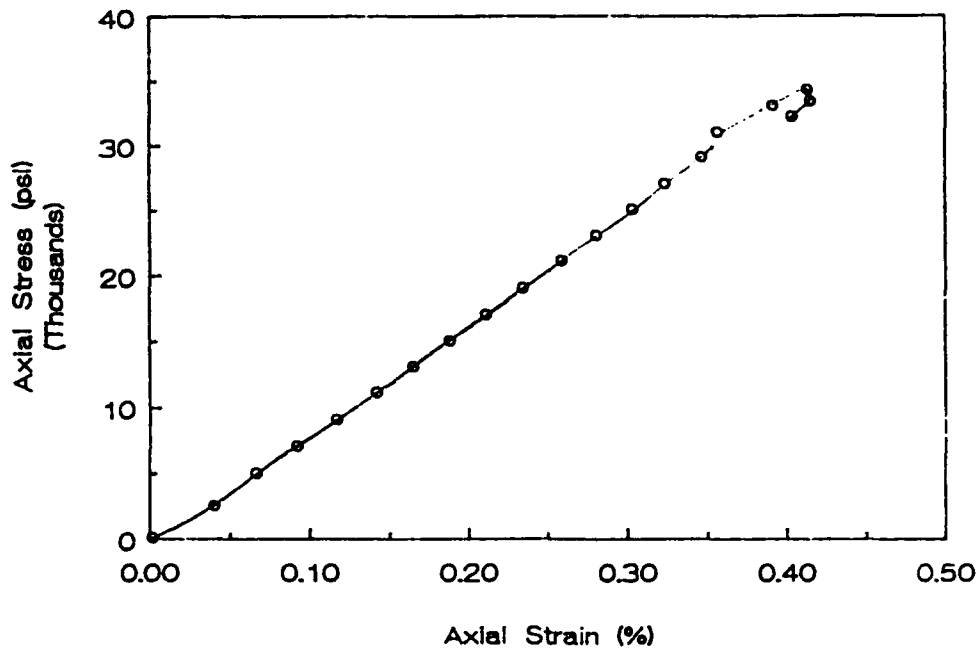


Figure 12. "Dynamic" stress-strain curve plot for a concrete sample, oriented vertically and subjected to a confining stress of 5000 psi. The plot was constructed from dynamic modulus calculated from the ultrasonic wave velocities.

5.3 Comparison of Static and Reconstructed Dynamic Stress-Strain Curves

In general, the reconstructed stress-strain curves show smaller axial strains. This is consistent with the tendency for dynamic moduli to be higher than static moduli. This is not the issue of import here. This phenomena is well established in the literature (King, 1980, for example). The issues of major importance is a qualitative determination of whether dynamic measurements are:

- (i) An accurate reflection of the relative number of microcracks present, and/or,
- (ii) Indicate catastrophic/permanent deformation.

As acoustical testing is commonly used to assess the presence of flaws, this is a particularly serious exercise. Initial observations tend to suggest that the shapes of the static and dynamic curves are similar. The indicators are qualitative only in this Phase I effort.

5.4 Photomicrograph

Figures 13a and 13b through Figures 17a and 17b are micrographic representations of the tests illustrated previously. In each case (a) is a photograph at a magnification of

approximately 12 times (the width of the photograph shown is one inch) and (b) is a trace of dominant microcrack features. A further observation relates to the differing microcrack spectrums, particularly different averages orientation between the limestone and the concrete. Table 1 details simple statistical processing of microcrack data from these samples, as a function of hydrostatic (and deviatoric) stress conditions.

5.5 Microcrack Observations

From Figures 13 through 17, it can be seen that most of the microcracks are extensile and are parallel or subparallel (small angle) to the direction of the maximum applied compressive stress. Table 1 shows that the average absolute angle between microcrack planes and the direction of the maximum applied compressive stress is less than 15° . The standard deviation for the angle with respect to the sample axis for all of the tested samples is $\sim 10^\circ$. In the limestone samples, the photomicrographs show that most microcracks propagate linearly except near their tips where they turn into slip planes of calcite crystals, just before they terminate.

Microcracks in the limestone appear to have been generated by more than one mechanism. However, these different mechanisms all relate to local tensile stress. Many microcracks were generated due to bending of long, beam-like grains (with their long axes parallel to bedding). In addition, contact point loading generated tensile stress concentrations which also generated extensile features. Tensile stress concentrations around an open pore space or a soft inclusion can also generate microcracks. Microcracks were found to have been generated from grain boundaries, especially those parallel to the direction of the maximum compression. In the concrete samples, most of the microcracks were generated from pore spaces and grain (aggregate) boundaries.

The density of the microcracks appears to increase as the confining stress is increased. The length distribution of microcracks is strongly dependent on the confining stress applied. At zero and low confining stress, microcracks apparently propagated farther than those generated under higher confining stress, before they were arrested. Interaction between microcracks occurs more readily at low confining stress because the microcracks are longer. This resulted in sample failure at relatively lower axial stresses. The decrease in microcrack length as the confining stress was increased is due to the stress intensity at crack tips. As indicated above, microcracks are generated by local tensile stresses which are usually concentrated at the origin of the microcracks. Propagation of these microcracks is driven by this local tensile stress. The confining stress (global compression) generates a negative stress intensity component counteracting the stress intensity factor due to the local tensile stress. As a result in these tests, confining stress reduces the stress intensity factor that propagates the microcracks. Hence, the average length of microcracks was reduced with an increase in confining stress.

In general, crack aperture (width) appears to be proportional to crack length, since the aperture of a crack is also proportional to stress intensity at crack tips. As can be seen

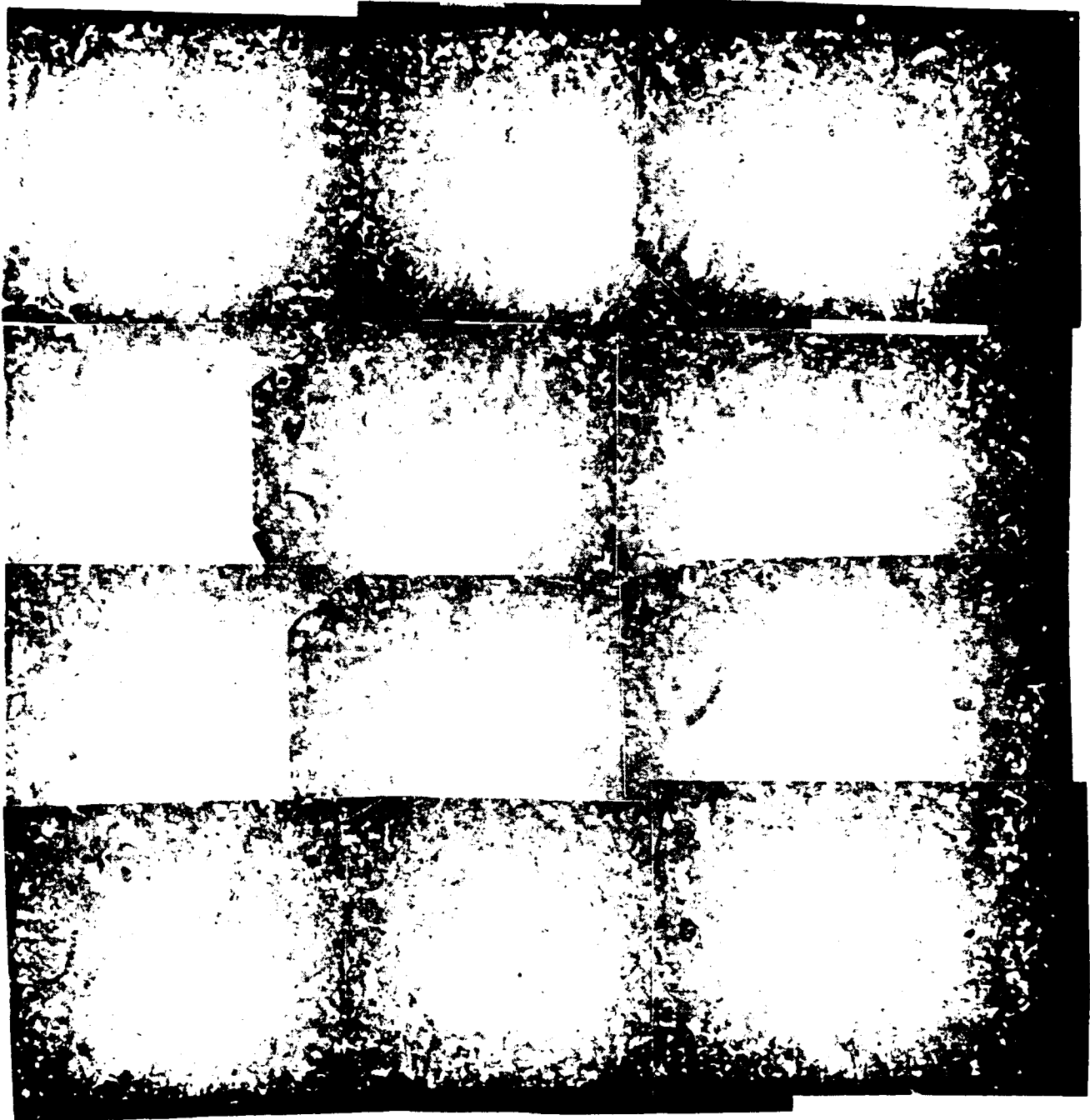


Figure 13a. Photomicrograph of an axial cross section Indiana limestone sample, subjected to a zero confining stress (post-peak). The width of the photomicrograph is the diameter of the sample and is one inch in dimension.

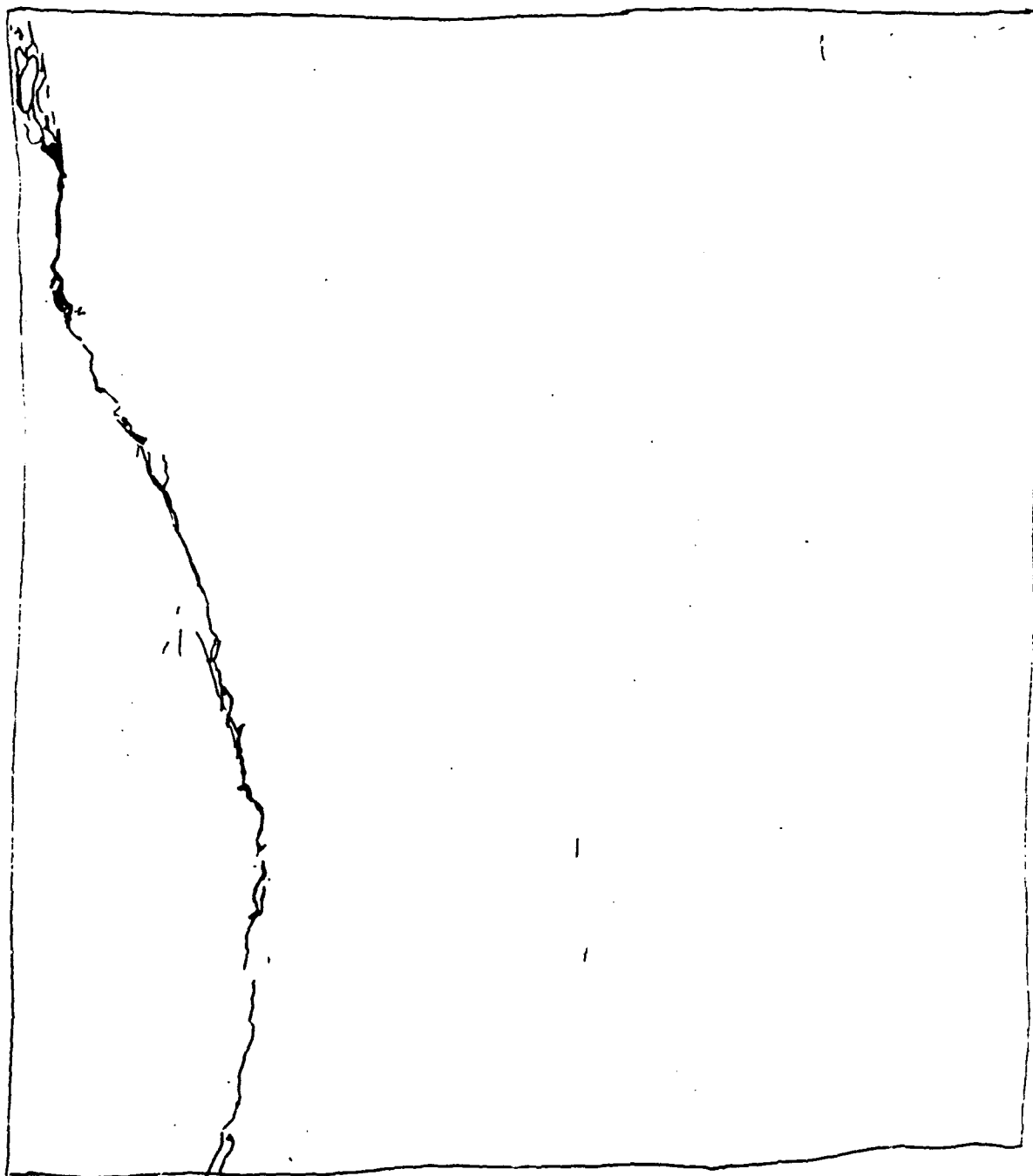


Figure 13b. Trace of dominant microcracks shown on the photomicrograph in Figure 13a.

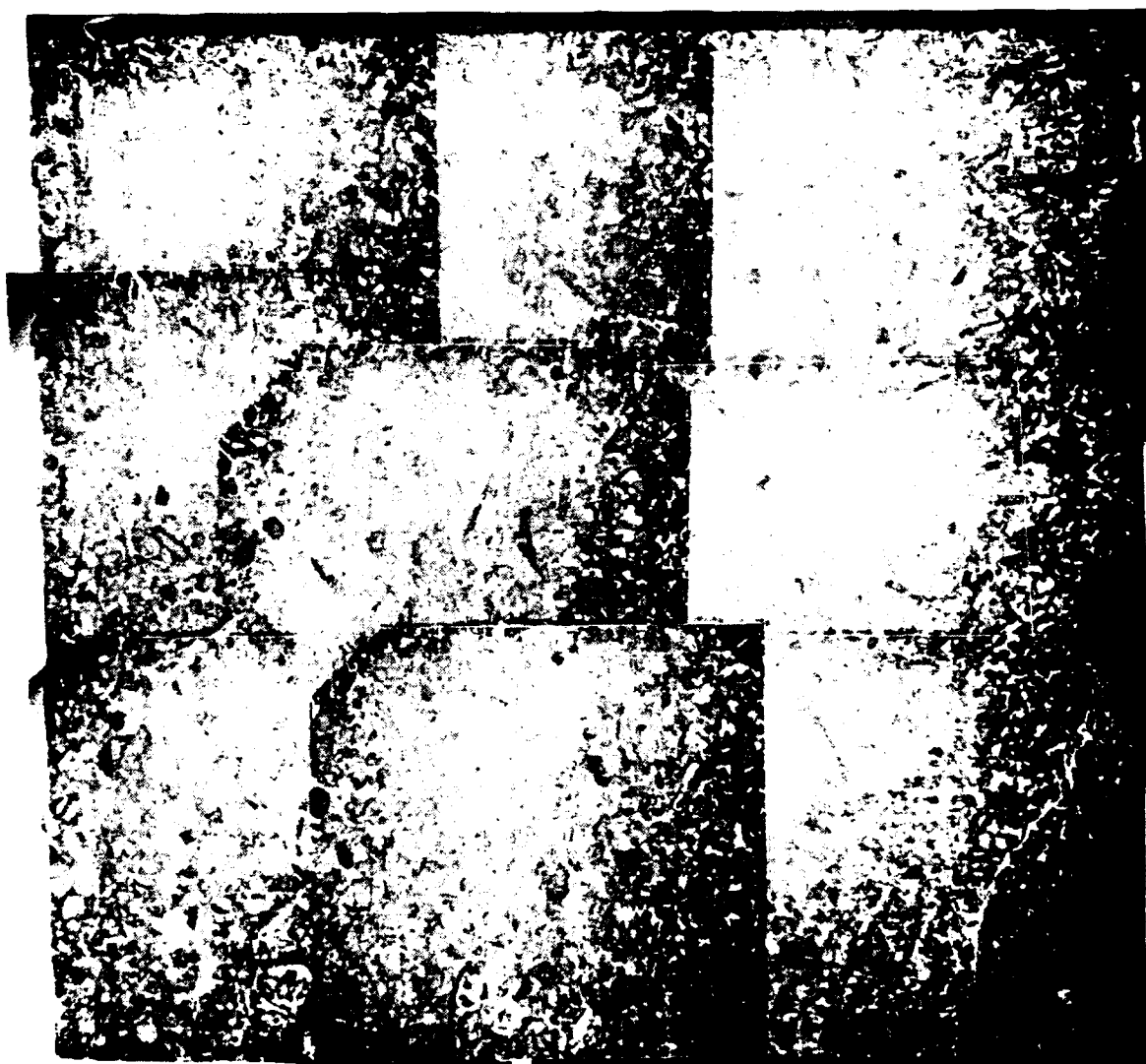


Figure 14a. Photomicrograph of an axial cross section Indiana limestone sample, subjected to a confining stress of 2500 psi (post-peak). The width of the photomicrograph is the diameter of the sample and is one inch in dimension.

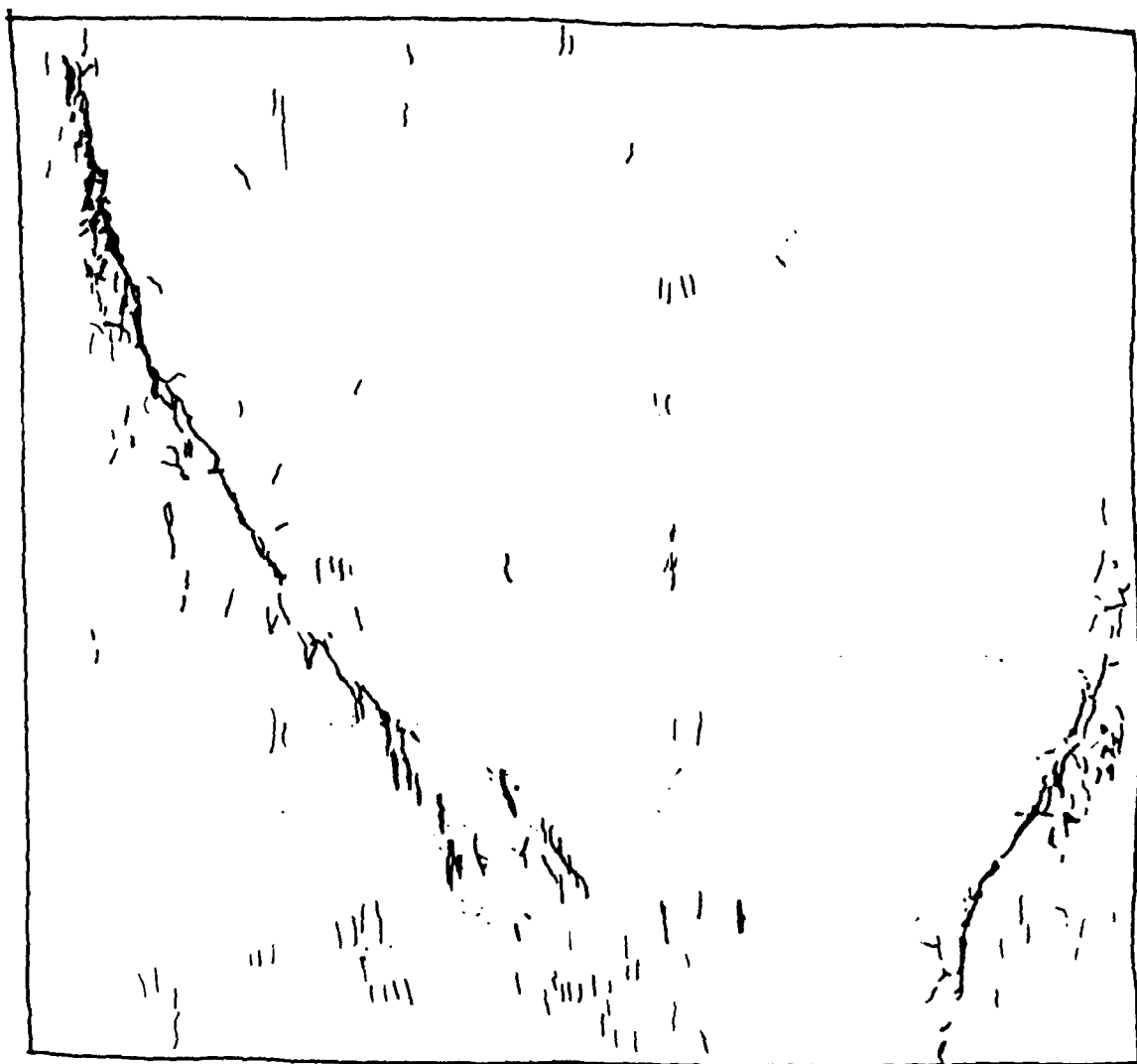


Figure 14b. Trace of dominant microcracks shown on the photomicrograph in Figure 14a.



Figure 15a. Photomicrograph of an axial cross section Indiana limestone sample, subjected to a confining stress of 5000 psi (post-peak). The width of the photomicrograph is the diameter of the sample and is one inch in dimension.

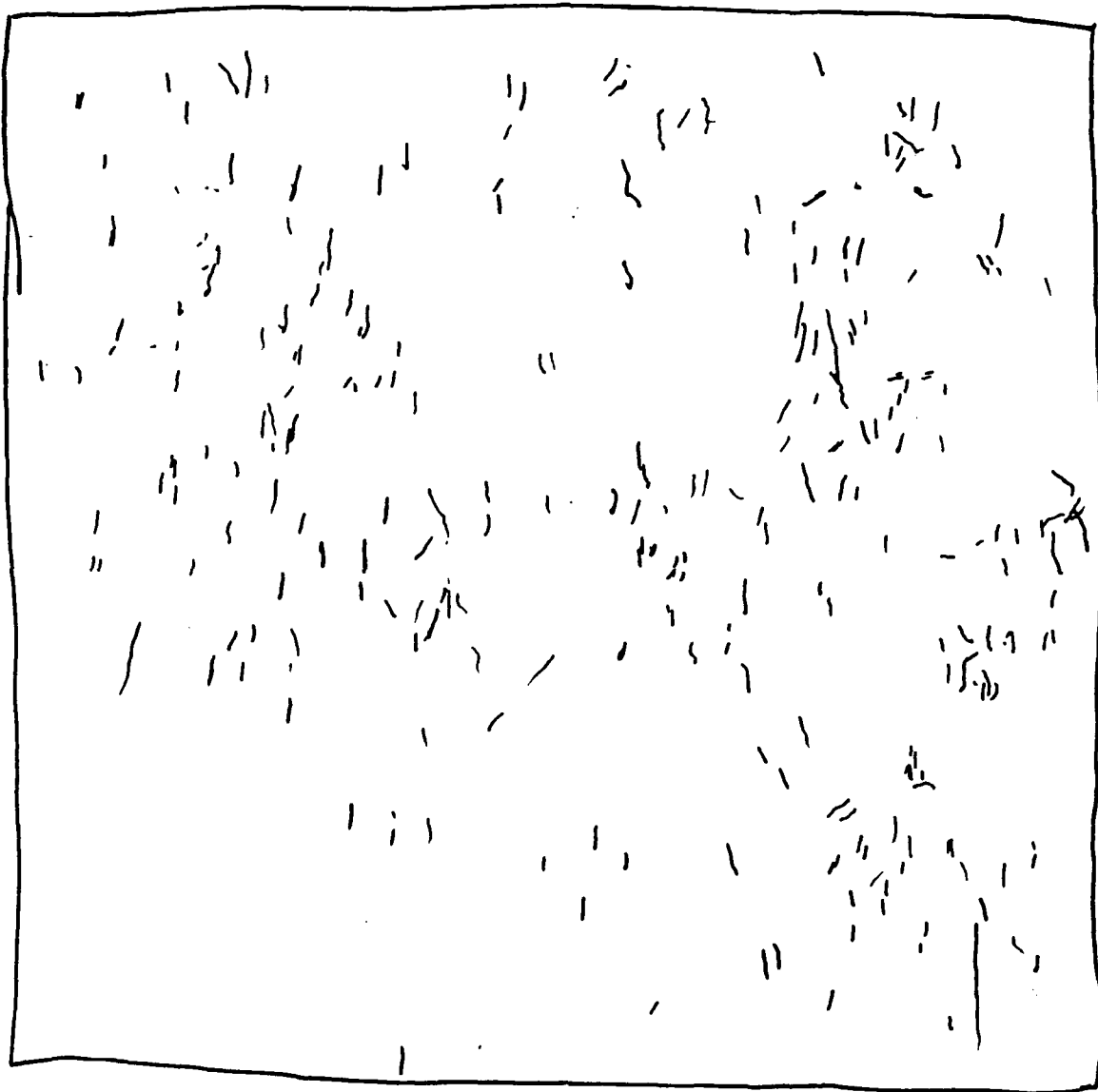


Figure 15b. Trace of dominant microcracks shown on the photomicrograph in Figure 15a.

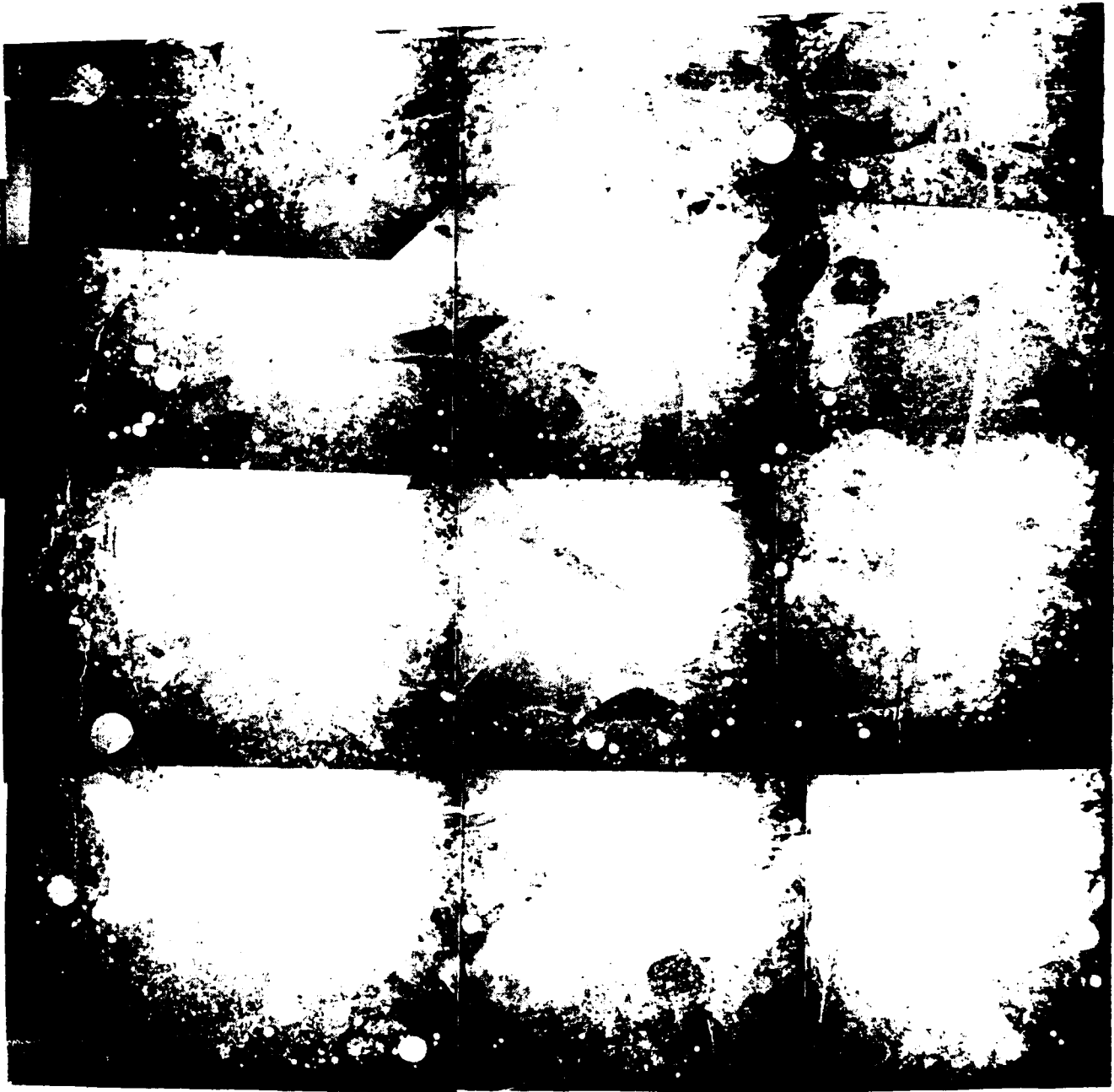


Figure 16a. Photomicrograph of an axial cross section of concrete sample, subjected to a zero confining stress (post-peak). The width of the photomicrograph is the diameter of the sample and is one inch in dimension.

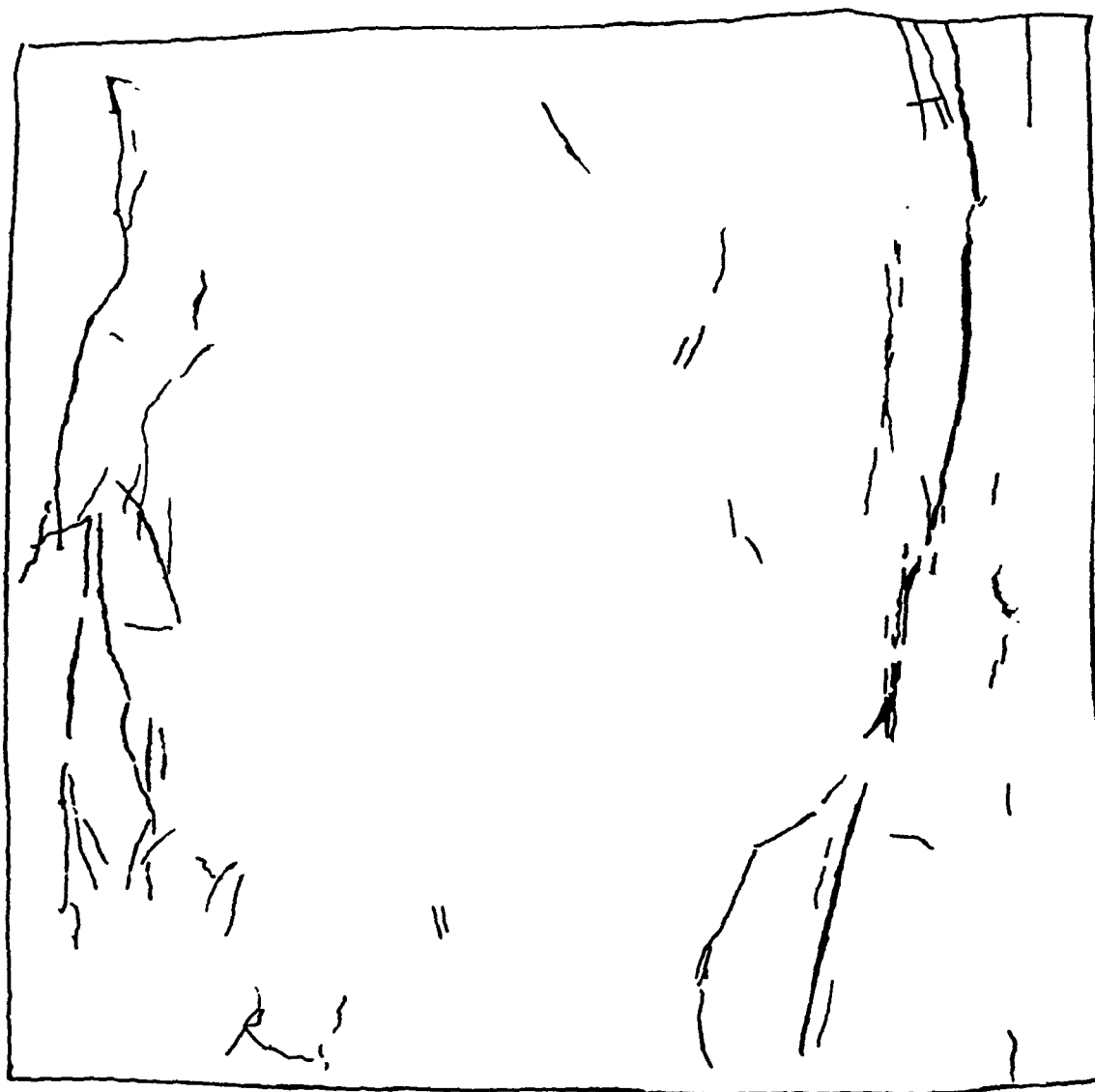


Figure 16b. Trace of dominant microcracks shown on the photomicrograph in Figure 16a.



Figure 17a. Photomicrograph of an axial cross section of concrete sample, subjected to a confining stress of 5000 psi (post-peak). The width of the photomicrograph is the diameter of the sample and is one inch in dimension.



Figure 17b. Trace of dominant microcracks shown on the photomicrograph in Figure 17a.

from Table 1, the crack aperture decreased with increasing confining stress. It appears that the average aspect ratio of microcracks (width to length ratio) in the limestone varies substantially but it was very consistent in concrete. This is a characteristic difference between the limestone and the concrete samples.

Microcrack interaction in the limestone was observed to occur in localized pattern. Under unconfined compression (Figures 3, 8 and 13), microcracks tended to connect with each other, form a longer extensile fracture which usually caused axial splitting. Under triaxial compression, where shear failure is in general the typical failure mode, it was observed that shear fractures were formed by many small extensile microcracks parallel to and offset from each other (Figures 5, 10 and 15). In concrete, however, no macro shear surfaces were observed and all samples failed in axial splitting. Most of the fractures were composed of a few smaller cracks but not as many as in the limestone.

5.6 "Dynamic" Stress-Strain Curves

The "dynamic" stress-strain curves, obtained from concurrent ultrasonic velocity measurements, were rather similar to those generated from conventional static stress-strain monitoring. It appears that these dynamic curves do not show the initial compaction evident in the static stress-strain curves. However, the "dynamic" stress-strain curves do show the generation and increase in density of microcracks. The measured changes in acoustic velocities are significant because they reflect the microstructural changes in the rock or the concrete. In combination with acoustic emission methods (recording acoustic events caused by generation of microcracks in a testing sample), it appears feasible that changes in the dynamic mechanical properties may be used for determination of microcrack density.

SBIR Microcrack Population

Sample Type	Confining Stress (psi)	Axial Stress at Failure (psi)	Microcrack Population					Pre-Microcrack		Poisson's Ratio	
			Density (crack/cm ²)	Length (mm)	Angle (degree)	Width (mm)	Aspect Ratio	Static (10 ⁶ psi)	Dynamic (10 ⁶ psi)	Static	Dynamic
LS 1	0	8190	5.735	1.144	80.3536	0.02513	0.02197	2.91	6.42	0.18	0.24
				1.279	9.7745	0.02147					
LS 2	2500	20180	28.06	0.8971	76.19	0.0221	0.0246	2.88	7.06	0.14	0.26
				0.7493	10.145	0.0317					
LS 3	5000	23320	30.69	0.7172	80.7273	0.01244	0.01735	3.66	7.00	0.16	0.26
				0.3268	10.2653	0.007714					
Con 1	0	12660	12.56	1.9866	77.9876	0.0239	0.01204	2.48	7.24	0.16	0.28
				2.0817	11.7223	0.02698					
Con 2	5000	34510	23.25	1.4256	80.8667	0.02051	0.01439	2.83	8.17	0.14	0.25
				1.4305	10.8811	0.01445					

Note: In columns marked "Length", "Angle" and "Width", the first line indicates average values of and the second line indicates the standard deviations of these quantities.

6 THEORETICAL CONSIDERATIONS ON MECHANICAL PROPERTY-MICROCRACK RELATIONSHIP

6.1 Background

The previous section on experimental observations provides qualitative representation of damage evolution. Beyond empirical observations, it is desirable to quantify the influence of "microcracks" in bulk material behavior. This is done in the following section, presuming elastic relationships and various presumptions on axes of symmetry.

6.2 CONSTITUTIVE EQUATIONS

An orthotropic, homogeneous and linear elastic material has different mechanical properties in three orthogonal directions. The constitutive relationship for such a material can be expressed in a 1, 2, 3 Cartesian coordinate system as follows:

$$\left\{ \begin{array}{l} \epsilon_{11} = \frac{1}{E_1} \sigma_{11} - \frac{\nu_{12}}{E_2} \sigma_{22} - \frac{\nu_{13}}{E_3} \sigma_{33} \\ \epsilon_{22} = -\frac{\nu_{21}}{E_1} \sigma_{11} + \frac{1}{E_2} \sigma_{22} - \frac{\nu_{23}}{E_3} \sigma_{33} \\ \epsilon_{33} = -\frac{\nu_{31}}{E_1} \sigma_{11} - \frac{\nu_{32}}{E_2} \sigma_{22} + \frac{1}{E_3} \sigma_{33} \\ \epsilon_{12} = 2G_3 \sigma_{12} \\ \epsilon_{23} = 2G_1 \sigma_{23} \\ \epsilon_{31} = 2G_2 \sigma_{31} \end{array} \right. \quad (3)$$

where ϵ_{ij} and σ_{ij} are the strain and stress components on the i plane, in the j direction; ν_{ij} is the deformation in i the direction induced by stress in the j direction due to Poisson's effect; E_i and G_i are Young's modulus and shear modulus in the i direction.

Equation (1) can be expressed in matrix form:

$$(\epsilon) = (A)(\sigma) = \begin{pmatrix} A_n & 0 \\ 0 & A_s \end{pmatrix} (\sigma) \quad (4)$$

where

$$A_n = \begin{pmatrix} \frac{1}{E_1} & \frac{-v_{12}}{E_2} & \frac{-v_{13}}{E_3} \\ \frac{-v_{21}}{E_1} & \frac{1}{E_2} & \frac{-v_{23}}{E_3} \\ \frac{-v_{31}}{E_1} & \frac{-v_{32}}{E_2} & \frac{1}{E_3} \end{pmatrix} \quad (2a)$$

and

$$A_s = \begin{pmatrix} \frac{1}{2G_3} & 0 & 0 \\ 0 & \frac{1}{2G_1} & 0 \\ 0 & 0 & \frac{1}{2G_2} \end{pmatrix} \quad (2b)$$

The inverse of the compliance matrix (A), often regarded as the stiffness matrix (C) can be expressed as:

$$(\sigma) = (A)^{-1}(\epsilon) = (C)(\epsilon) = \begin{pmatrix} C_n & 0 \\ 0 & C_s \end{pmatrix} (\epsilon) \quad (3)$$

This matrix exists if and only if the compliance matrix is symmetric. As a result, the following relationships exist:

$$\frac{v_{13}}{E_3} = \frac{v_{31}}{E_1}; \frac{v_{23}}{E_3} = \frac{v_{32}}{E_2} \text{ and } \frac{v_{12}}{E_2} = \frac{v_{21}}{E_1} \quad (4)$$

Matrices (C_n) and (C_s) are the inverse matrices of (A_n) and (A_s), respectively:

$$(C_s) = (A_s)^{-1} = \begin{pmatrix} 2G_3 & 0 & 0 \\ 0 & 2G_1 & 0 \\ 0 & 0 & 2G_2 \end{pmatrix} \quad (5a)$$

and

$$(C_n) = (A_n)^{-1} = \begin{pmatrix} C_{11} & C_{12} & C_{13} \\ C_{21} & C_{22} & C_{23} \\ C_{31} & C_{32} & C_{33} \end{pmatrix} \quad (5b)$$

where

$$\begin{aligned} C_{11} &= \frac{E_1}{C_0} (1 - \nu_{23} \nu_{32}) \\ C_{12} &= \frac{E_1}{C_0} (\nu_{12} + \nu_{13} \nu_{32}) \\ C_{13} &= \frac{E_1}{C_0} (\nu_{13} + \nu_{12} \nu_{23}) \\ C_{21} &= \frac{E_2}{C_0} (\nu_{21} + \nu_{23} \nu_{31}) \\ C_{22} &= \frac{E_2}{C_0} (1 - \nu_{13} \nu_{31}) \\ C_{23} &= \frac{E_2}{C_0} (\nu_{23} + \nu_{21} \nu_{13}) \\ C_{31} &= \frac{E_3}{C_0} (\nu_{31} + \nu_{32} \nu_{21}) \\ C_{32} &= \frac{E_3}{C_0} (\nu_{32} + \nu_{31} \nu_{12}) \\ C_{33} &= \frac{E_3}{C_0} (1 - \nu_{12} \nu_{21}) \end{aligned} \quad (5c)$$

and

$$C_0 = 1 - \nu_{12} \nu_{23} \nu_{31} - \nu_{21} \nu_{32} \nu_{13} - \nu_{13} \nu_{21} \nu_{12} - \nu_{13} \nu_{31} \nu_{23} \nu_{32} \quad (5d)$$

6.3 EQUILIBRIUM EQUATIONS⁴

The equilibrium equations for an elastic material in the absence of body forces can be written as follows:

⁴For more information, refer to Jaeger and Cook, 1976.

$$\begin{aligned}
\frac{\partial \sigma_{11}}{\partial x_1} + \frac{\partial \sigma_{12}}{\partial x_2} + \frac{\partial \sigma_{13}}{\partial x_3} &= \rho \frac{\partial^2 u_1}{\partial t^2} \\
\frac{\partial \sigma_{21}}{\partial x_1} + \frac{\partial \sigma_{22}}{\partial x_2} + \frac{\partial \sigma_{23}}{\partial x_3} &= \rho \frac{\partial^2 u_2}{\partial t^2} \\
\frac{\partial \sigma_{31}}{\partial x_1} + \frac{\partial \sigma_{32}}{\partial x_2} + \frac{\partial \sigma_{33}}{\partial x_3} &= \rho \frac{\partial^2 u_3}{\partial t^2}
\end{aligned} \tag{6}$$

Where u_i is the displacement of a point in direction i ; x_i is an independent variable (unit) in direction i ; t is the time and ρ is the density of the material.

The strain ϵ_{ij} is:

$$\begin{aligned}
\epsilon_{11} &= \frac{\partial u_1}{\partial x_1} \\
\epsilon_{22} &= \frac{\partial u_2}{\partial x_2} \\
\epsilon_{33} &= \frac{\partial u_3}{\partial x_3} \\
\epsilon_{12} &= \frac{1}{2} \left(\frac{\partial u_1}{\partial x_2} + \frac{\partial u_2}{\partial x_1} \right) \\
\epsilon_{23} &= \frac{1}{2} \left(\frac{\partial u_2}{\partial x_3} + \frac{\partial u_3}{\partial x_2} \right) \\
\epsilon_{31} &= \frac{1}{2} \left(\frac{\partial u_3}{\partial x_1} + \frac{\partial u_1}{\partial x_3} \right)
\end{aligned} \tag{7}$$

To calculate dynamic properties for an elastic material, the displacement components u_i can be assumed to be presented as:

$$\begin{aligned}
u_1 &= B_1 f(x_1 \cos \alpha_1 + Ct) \\
u_2 &= B_2 f(x_2 \cos \alpha_2 + Ct) \\
u_3 &= B_3 f(x_3 \cos \alpha_3 + Ct)
\end{aligned} \tag{8}$$

In equation (8), B_i is a constant, α_i is the angle of incidence of an elastic wave with respect to the normal of plane i (direction i), and C is the velocity of the elastic wave.

6.4 ELASTIC WAVE MOTION EQUATION

By bringing (3) and (7) into (6), one can obtain the motion equation for an elastic wave:

$$\begin{aligned} D_{11} B_{11} + D_{12} B_{12} + D_{13} B_{13} &= \rho C^2 B_1 \\ D_{21} B_{21} + D_{22} B_{22} + D_{23} B_{23} &= \rho C^2 B_2 \\ D_{31} B_{31} + D_{32} B_{32} + D_{33} B_{33} &= \rho C^2 B_3 \end{aligned} \quad (9)$$

where

$$\begin{aligned} D_{11} &= C_{11} \cos^2 \alpha_1 + G_3 \cos^2 \alpha_2 + G_2 \cos^2 \alpha_3 \\ D_{22} &= C_{22} \cos^2 \alpha_2 + G_1 \cos^2 \alpha_3 + G_3 \cos^2 \alpha_1 \\ D_{33} &= C_{33} \cos^2 \alpha_3 + G_1 \cos^2 \alpha_2 + G_2 \cos^2 \alpha_1 \\ D_{12} &= (C_{12} + G_3) \cos \alpha_1 \cos \alpha_2 \\ D_{23} &= (C_{23} + G_1) \cos \alpha_2 \cos \alpha_3 \\ D_{31} &= (C_{31} + G_2) \cos \alpha_3 \cos \alpha_1 \end{aligned} \quad (9a)$$

The wave motion equations (9) can be written in matrix form:

$$(D - \rho C^2)(B) = (0) \quad (10)$$

or

$$\begin{pmatrix} D_{11} - \lambda & D_{12} & D_{13} \\ D_{21} & D_{22} - \lambda & D_{23} \\ D_{31} & D_{32} & D_{33} - \lambda \end{pmatrix} \begin{pmatrix} B_1 \\ B_2 \\ B_3 \end{pmatrix} = (0) \quad (11)$$

where $\lambda = \rho C^2$.

A set of non-zero solutions for (10) or (11) exists if and only if the determinant of the coefficient matrix of equation (11) equals zero, i.e.,

$$\begin{vmatrix} D_{11} - \lambda & D_{12} & D_{13} \\ D_{21} & D_{22} - \lambda & D_{23} \\ D_{31} & D_{32} & D_{33} - \lambda \end{vmatrix} = 0 \quad (12)$$

or

$$-\lambda^3 + I_1 \lambda^2 + I_2 \lambda + I_3 = 0 \quad (13)$$

where

$$I_1 = D_{11} + D_{22} + D_{33}$$

$$I_2 = - \begin{vmatrix} D_{11} & D_{12} \\ D_{21} & D_{22} \end{vmatrix} - \begin{vmatrix} D_{22} & D_{23} \\ D_{32} & D_{33} \end{vmatrix} - \begin{vmatrix} D_{33} & D_{31} \\ D_{13} & D_{11} \end{vmatrix} \quad (13a)$$

$$I_3 = \begin{vmatrix} D_{11} & D_{12} & D_{13} \\ D_{21} & D_{22} & D_{23} \\ D_{31} & D_{32} & D_{33} \end{vmatrix}$$

The values of λ which satisfy equations (12) or (13) are *eigenvalues* of equation (11). The velocities C of elastic waves can be obtained from $C = \sqrt{\lambda/\rho}$, once the *eigenvalues* λ are obtained.

6.5 ELASTIC RELATIONS FOR AN AXISYMMETRICALLY MICROCRACKED MATERIAL

Relations outlined in previous sections are well known. The following derivations incorporate microcracking. Restricting consideration to microcracks generated in a homogeneous, isotropic and elastic material under triaxial compression ($\sigma_1 > \sigma_2 = \sigma_3$), the elastic properties of this cracked (damaged) material can be considered to be axisymmetric and the elastic modulus in the axial direction is presumed not to be changed. The elastic properties of this material are:

$$\begin{aligned} E_1 &= E \text{ (known, same as for the original uncracked (undamaged) material), } E_2 = E_3 \\ v_{21} &= v_{31} = v \text{ (known, same as the uncracked (undamaged) material), } v_{12} = v_{13}, v_{23} = v_{32} \\ G_1, G_2 &= G_3 \end{aligned} \quad (14)$$

Using (14) in the constitutive equations (2a) and (2b), and (5a) and (5b); one can obtain:

$$\begin{aligned} C_0 &= 1 - 2v_{12}v_{21}v_{23} - v_{23}^2 - 2v_{12}v_{21} \\ &= 1 - v_{23}^2 - 2v_{12}v_{21}(v_{23} + 1) \\ &= 1 - v_{23}^2 - 2v_{12}^2(v_{23} + 1) \frac{E}{E_2} \\ &= 1 - v_{23}^2 - 2v^2(v_{23} + 1) \frac{E_2}{E} \end{aligned} \quad (15a)$$

and

$$\begin{cases}
C_{11} = \frac{E}{C_0}(1 - \nu_{23}^2) \\
C_{12} = \frac{E}{C_0}\nu_{12}(1 + \nu_{23}) = \frac{E_2}{C_0}\nu(1 + \nu_{23}) \\
C_{13} = \frac{E}{C_0}\nu_{12}(1 + \nu_{23}) = C_{12} \\
C_{21} = \frac{E_2}{C_0}\nu_{21}(1 + \nu_{23}) = \frac{E_2}{C_0}\nu(1 + \nu_{23}) \\
C_{22} = \frac{E_2}{C_0}(1 - \nu_{13}\nu_{31}) = \frac{E_2}{C_0}(1 - \nu\nu_{12}) \\
C_{23} = \frac{E_2}{C_0}(\nu_{23} + \nu\nu_{12}) \\
C_{31} = \frac{E_3}{C_0}\nu_{31}(1 + \nu_{23}) = C_{21} \\
C_{32} = \frac{E_3}{C_0}(\nu_{23} + \nu_{31}\nu_{13}) = C_{23} \\
C_{33} = \frac{E_3}{C_0}(1 - \nu_{12}\nu_{21}) = \frac{E_2}{C_0}(1 - \nu\nu_{12})
\end{cases} \quad (15b)$$

$$\text{and } \frac{\nu_{12}}{E_2} = \frac{\nu_{21}}{E} = \frac{\nu}{E} \text{ or } \frac{E}{E_2} = \frac{\nu}{\nu_{12}}$$

6.6 ELASTIC CONSTRAINT (ENERGY CONSERVATION) FOR AN ISOTROPIC MATERIAL WITH AN ANISOTROPIC EXTENSILE MICROCRACK DISTRIBUTION

The principles of superposition and energy conservation can be used to derive the elastic constants for an isotropic material containing preferentially distributed (oriented) extensile cracks (Figure 18), as defined in section 4.4.

Using energy conservation principles:

$$U'_e = U_e + Nu_c \quad (16)$$

where U'_e is the total strain energy in the cracked (damaged) material, U_e is the total energy for the uncracked material, N is the total number of cracks and u_c is the strain energy of a single crack. U'_e and U_e are functions of the applied stress and elastic properties of the material:

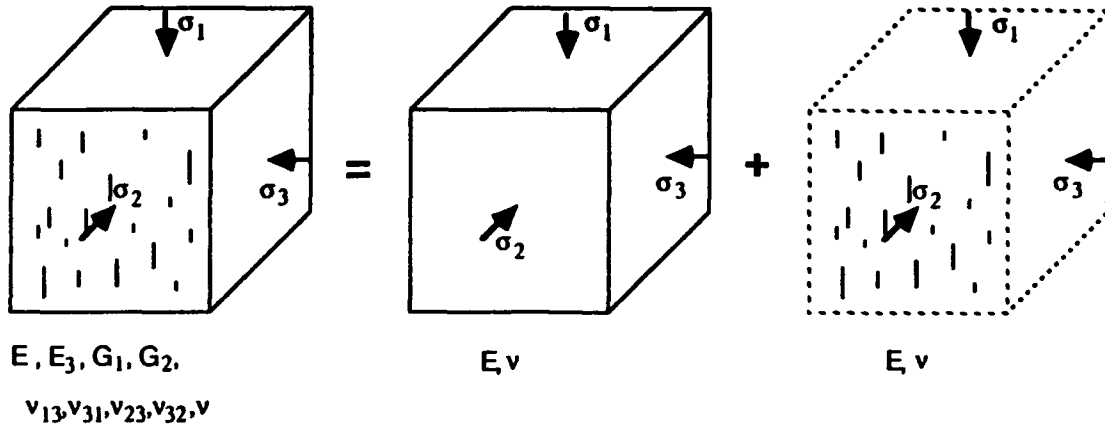


Figure 18. Schematic representation of the principles of superposition applied to a material containing microcracks.

$$U_e' = \frac{V}{2} \sigma' \epsilon' (E_1, E_2, E_3, G_1, G_2, G_3, \nu_{12}, \nu_{23}, \nu_{31}) \quad (17a)$$

and

$$U_e = \frac{V}{2} \sigma \epsilon (E, \nu) \quad (17b)$$

where V is the volume of the material and all the variables in parentheses are elastic properties of a cracked material (17a) and the original uncracked material (17b).

Presume that typical microcrack morphology is penny shaped. The strain energy around a penny-shaped crack (Figure 19) can be expressed as the energy per unit area of the crack:

$$J = \frac{K_I^2(1-\nu^2)}{E} + \frac{K_{II}^2(1-\nu^2)}{E} + \frac{K_{III}^2(1+\nu)}{E} \quad (18)$$

where J is the energy released per unit crack surface area generated, K_I , K_{II} , and K_{III} are the stress intensity factors for Mode I, II and III crack surface displacements.

Using (17) and (18) into (16) one obtains:

$$\frac{V}{2}\sigma_{ii}'\epsilon_{ii}' = \frac{V}{2}\sigma_{ii}\epsilon_{ii} + N \int_A J dA \quad (19)$$

where A is the surface area of a single crack.

6.7 STRAIN ENERGY FOR A PENNY-SHAPED CRACK

The stress intensity factors for a penny-shaped crack under uniform tensile and shear stress (Figure 19) are as follows:

$$\begin{aligned} \sigma_z &= -\sigma_0 \\ \tau_{zx} \text{ (or } \tau_{zy}) &= \tau_{12} \text{ (or } \tau_{13}) = \tau_0 \\ \tau_{xy} &= \tau_{23} = \tau_0 \\ \left\{ \begin{aligned} K_I &= \frac{2}{\pi} \sigma_0 \sqrt{a} \\ K_{II} &= \frac{1}{2-\nu} \frac{4}{\pi} \tau_0 \sqrt{a} \sin \theta \\ K_{III} &= \frac{1-\nu}{2-\nu} \frac{4}{\pi} \tau_0 \sqrt{a} \cos \theta \end{aligned} \right. \quad (20) \end{aligned}$$

where a is the radius of the penny-shaped crack, τ_{12} (or τ_{13}) is the uniform shear stress acting on planes 2 (or 3) in the direction of 1, σ_0 is the uniform tension orthogonal to the crack plane, τ_{23} is the uniform shear stress on the crack plane and θ is the on the crack plane angle from direction 2 to the point of consideration.

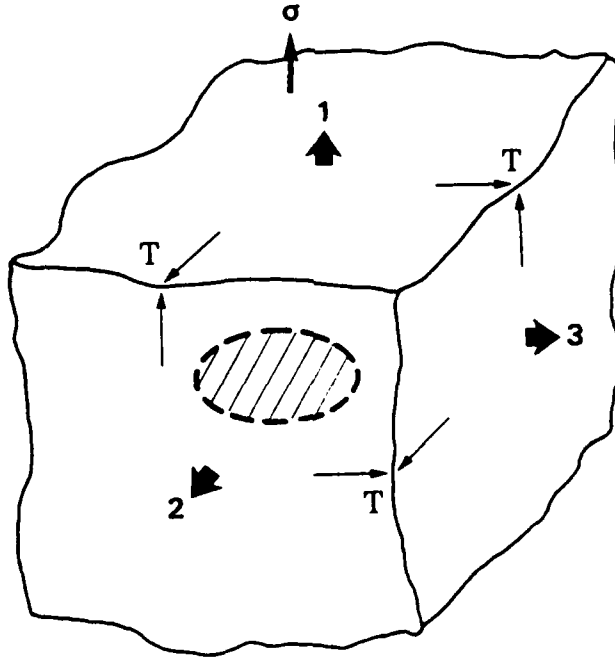


Figure 19. Penny-shaped crack in an infinite body under uniform tension and shear.

The strain energy around this single crack is:

$$\begin{aligned}
 u_c &= \int_0^a 2J\pi a da \\
 &= 2\pi \int_0^a \left(\frac{1-\nu^2}{E} K_I^2 + \frac{1-\nu^2}{E} K_{II}^2 + \frac{1+\nu}{E} K_{III}^2 \right) a da \\
 &= \frac{2\pi(1-\nu^2)}{E} \int_0^a \left(K_I^2 + K_{II}^2 + \frac{K_{III}^2}{1-\nu} \right) a da
 \end{aligned} \tag{21}$$

These energy relationships will be used in subsequent sections for delineating effective modulus.

Using (20) in (21), one obtains:

$$u_c = \frac{16a^3(1-\nu^2)}{3E} \left(\sigma_0^2 + \frac{2(2+\nu^2)}{(2-\nu)(1-\nu)} \tau_0^2 \right) \tag{22}$$

6.8 ELASTIC (P AND S) WAVE PROPAGATION

During compressional (P) wave propagation through an elastic medium, the medium is effectively subjected to uniaxial elastic strain, that is, if the P-wave is parallel to direction i , then,

$$\epsilon_{ii} \neq 0, \epsilon_{jj} = \epsilon_{kk} = 0, j \neq i, k \neq i$$

In the following subsections, P and S wave propagation in a material with axisymmetrically distributed cracks (generated from triaxial compression) are evaluated. Wave propagation in different principal directions is considered.

6.8.1 P-Wave Propagating in Direction 1

In this case, the material is subjected to uniaxial strain in direction 1:

$$i = 1, \epsilon_{11} = \frac{(1-\nu-2\nu^2)}{(1-\nu)E} \sigma_{11}, \epsilon_{22} = \epsilon_{33} = \epsilon_{12} = \epsilon_{23} = \epsilon_{31} = 0$$

and

$$\sigma_{22} = \sigma_{33} = \frac{\nu}{1-\nu} \sigma_{11} \tag{23}$$

in the virgin, undamaged material. In the microcracked medium,

$$i=1, \epsilon_{22}' = \epsilon_{33}' = \epsilon_{12}' = \epsilon_{23}' = \epsilon_{31}' = 0$$

and

$$\epsilon_{11}' = \frac{\sigma_{11}'}{C_{11}} = \frac{\sigma_{11}' C_0}{E(1-\nu_{23}^2)} \quad (24)$$

$$\sigma_{22}' = \sigma_{33}' = \frac{\nu_{12}}{1-\nu_{23}} \sigma_{11}' \quad (25)$$

where

$$C_0 = 1 - \nu_{23}^2 - 2 \frac{E}{E_2} \nu^2 (1 + \nu_{23}) \quad (26)$$

$$\frac{V}{2} \sigma_{ii}' \epsilon_{ii}' = \frac{V(1-\nu-2\nu^2)}{2(1-\nu)E} \sigma_{11}^2 \quad (27)$$

$$\frac{N}{2} \sigma_{ii}' \epsilon_{ii}' = \frac{V}{2} \frac{C_0}{E(1-\nu_{23}^2)} \sigma_{11}^2 \quad (28)$$

The normal and shear stresses applied on a crack whose normal is oriented at ϕ from direction 2 are:

$$\begin{cases} \sigma_\phi = \frac{\nu}{1-\nu} \sigma_{11} \\ \tau_\phi = 0 \end{cases} \quad (29)$$

Assuming that N cracks are homogeneously distributed with angle ϕ varying from 0 to 360° (axisymmetric), the total strain energy for the microcracks can be expressed as:

$$U_c = \int_0^\pi \frac{N}{\pi} u_c d\phi \quad (30)$$

The energy conservation equation (19) yields:

$$\frac{1}{2} \sigma_{ii}' \epsilon_{ii}' = \frac{1}{2} \sigma_{ii}' \epsilon_{ii}' + \int_\pi^0 \frac{N}{\pi V} U_c d\phi \quad (31)$$

Using equations (27), (28), (29), and (22) in (31), gives:

$$\frac{\sigma_{11}^2 C_0}{2E(1-\nu_{23}^2)} = \frac{\sigma_{11}^2 (1-\nu-2\nu^2)}{2E(1-\nu)} + \int_0^\pi \frac{N}{\pi V} \frac{16a^3(1-\nu^2)}{3E} \sigma_\phi^2 d\phi \quad (32)$$

and

$$\frac{C_0}{2(1-v_{23}^2)} = \frac{1-v-2v^2}{2(1-v)} + \frac{N}{V} \frac{16a^3(1+v)}{3} \frac{v^2}{1-v} \quad (33)$$

These equations will be used later to solve for effective moduli and Poisson's ratios.

6.8.2 Shear (S) Wave Traveling in Direction 1: (Particle Motion in a Plane with its Normal Parallel to Direction 1)

Assuming that a shear (S) wave (with magnitude τ) travels in direction 1 and vibrates with an angle α to direction 2, the stresses on a crack at an angle ϕ to direction 2 are:

$$\begin{cases} \sigma_\phi = 0 \\ \tau_\phi = \tau \end{cases} \quad (34)$$

The energy conservation principle (19) gives:

$$\frac{\tau^2}{2G_1} = \frac{\tau^2}{2G} + \frac{32Na^3(1+v)(2+v^2)}{3VE(2-v)} \tau^2 \quad (35)$$

$$\frac{1}{2G_1} = \frac{1}{2G} + \frac{32\chi(1+v)(2+v^2)}{3E(2-v)} \quad (36)$$

where

$$\chi = \frac{Na^3}{V} = \text{crack density (dimensionless)}$$

6.8.3 P and S Wave Traveling Orthogonal to Direction 1

The following example presumes a wave propagating in direction 2. Derivations for other "radial" directions are analogous because of symmetry conditions. When a P-wave (with magnitude σ_{22}) is propagating in direction 2, the material is subjected to uniaxial strain in direction 2.

$$\begin{aligned} i=2 \\ \epsilon_{11} = \epsilon_{33} = \epsilon_{11}' = \epsilon_{33}' = 0 \\ \epsilon_{22} = \frac{\sigma_{22}}{E} \left(1 - \frac{2v^2}{1-v} \right) \\ \epsilon_{22}' = \frac{\sigma_{22}}{C_{22}} = \frac{\sigma_{22} C_0}{E_2(1-Kv^2)} \end{aligned} \quad (37)$$

$$\begin{aligned}
\sigma_{11} &= \sigma_{33} = \frac{\nu}{1-\nu} \sigma \\
\sigma_{11}' &= C_{12} \epsilon_{22}' = K \frac{\nu(1+\nu_{23})}{(1-K\nu^2)} \sigma_{22} \\
\sigma_{33}' &= C_{32} \epsilon_{22}' = \frac{(\nu_{23}+K\nu^2)}{1-K\nu^2} \sigma_{22} \\
\tau_{12} &= \tau_{23} = \tau_{13} = 0
\end{aligned} \tag{38}$$

where

$$K = \frac{E}{E_2}$$

When a shear (S) wave is traveling (with magnitude τ) in direction 2 and vibrates with an angle α to direction 1, the stress components τ_{12} , τ_{13} , and τ_{23} are

$$\begin{cases} \tau_{12} = \tau \cos \alpha \\ \tau_{23} = \tau \sin \alpha \\ \tau_{13} = 0 \end{cases} \tag{39}$$

Stresses acting on a fracture plane, refer to Figure 20, are:

$$\begin{cases} \sigma_\phi = \frac{\sigma_{22} + \sigma_{33}}{2} + \frac{\sigma_{22} - \sigma_{33}}{2} \cos 2\phi + \tau_{23} \sin 2\phi \\ \tau_\phi = \frac{\sigma_{22} - \sigma_{33}}{2} \sin 2\phi + \tau_{23} \cos 2\phi \\ \tau_z = \tau_{13} \sin \phi + \tau_{12} \cos \phi \end{cases} \tag{40}$$

The energy conservation equation becomes:

$$\frac{\sigma^2 C_0 K}{2E(1-K\nu^2)} = \frac{\sigma^2}{2E} \left(1 - \frac{2\nu^2}{1-\nu}\right) + \frac{2N}{\pi V} \int_0^{\frac{\pi}{2}} u_c(\sigma_\phi, \tau_\phi, \tau_z) d\phi \tag{41}$$

and

$$\frac{\tau^2}{2} \left(\frac{\cos^2 \alpha}{G_2} + \frac{\sin^2 \alpha}{G_1} \right) = \frac{\tau^2}{2G} + \frac{2N}{\pi V} \int_0^{\frac{\pi}{2}} u_c(\sigma_\phi, \tau_\phi, \tau_\phi) d\phi \tag{42}$$

Using equations (38), (39) and (40) in (41) and (42), one obtains:

$$\frac{\sigma^2 C_0 K}{2E(1-K\nu^2)} = \frac{\sigma^2}{2E} \left(1 - \frac{2\nu^2}{1-\nu}\right) + \frac{2N}{\pi V} \int_0^{\frac{\pi}{2}} \frac{16a^3(1-\nu^2)}{3E} \frac{\sigma^2}{4(1-\nu)^2} \left((1+(1-2\nu)\cos 2\phi)^2 + 2 \frac{(2+\nu^2)(1-2\nu)^2}{(2-\nu)(1-\nu)} \sin^2 \phi \right) d\phi$$

or

$$\frac{C_0 K}{2E(1-K\nu^2)} = \frac{1}{2E} \left(1 - \frac{2\nu^2}{1-\nu}\right) + \frac{4\chi(1+\nu)}{3E(1-\nu)} \left(1 + \frac{(1-2\nu)^2}{2} + \frac{(2+\nu)(1-2\nu)^2}{(2-\nu)(1-\nu)} \right) \quad (43)$$

and

$$\frac{\tau^2}{2} \left(\frac{\cos^2 \alpha}{G_2} + \frac{\sin^2 \alpha}{G_1} \right) = \frac{\tau^2}{2G} + \frac{2N}{\pi V} \int_0^{\frac{\pi}{2}} \frac{16a^3(1-\nu^2)}{3E} (\tau^2 \sin^2 \alpha \sin^2 2\phi + \frac{2(2+\nu^2)}{(2-\nu)(1-\nu)} \tau^2 (\cos^2 \phi \cos^2 \alpha + \cos^2 2\phi \sin^2 \alpha)) d\phi \quad (44)$$

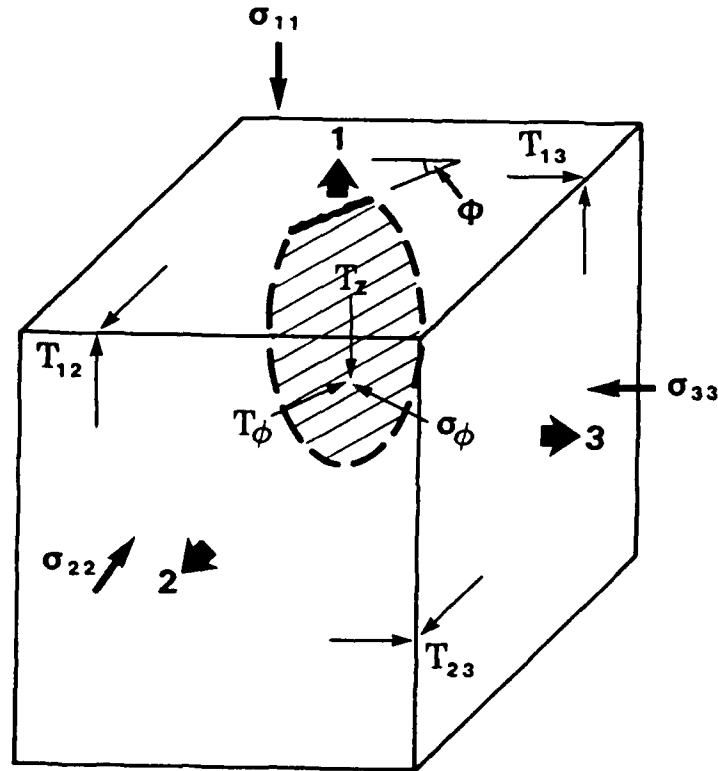


Figure 20. Stresses acting on a penny-shaped crack whose normal is orthogonal to direction 1 and at an angle ϕ to direction 2.

Because the incidence angle α varies from 0 to π , (44) becomes (after integration with respect to α):

$$\frac{1}{4} \left(\frac{1}{G_2} + \frac{1}{G_1} \right) = \frac{1}{2G} + \frac{4Na^3(1+v)(10-3v+5v^2)}{3EV(2-v)} \quad (45)$$

or

$$\frac{1}{4} \left(\frac{1}{G_1} + \frac{1}{G_2} \right) = \frac{1}{2G} + \frac{2\chi(10-3v+5v^2)}{3G(2-v)}$$

Solving (33), (36), (43) and (45) simultaneously gives the effective mechanical properties of a multiple-cracked material:

$$\frac{1}{G_1} = \frac{1}{G} \left(1 + \frac{32\chi(2+v^2)}{3(2-v)} \right) \quad (46)$$

or

$$G_1 = \frac{G}{1 + \frac{32\chi(2+v^2)}{3(2-v)}}$$

$$\frac{1}{G_2} = \frac{1}{G} \left(1 + \frac{8\chi(2-v+v^2)(1+v)}{3(2-v)} \right) \quad (47)$$

or

$$G_2 = \frac{G}{1 + \frac{8\chi(2-v+v^2)(1+v)}{3(2-v)}}$$

$$\begin{aligned} & 2(1-v_{23})^2(1+v_{23})v^2(3-8(1+v)\chi)(3-3v-6v^2+16(1+v)\chi) \\ & = (1-v-(1-v_{23})v^2(3-8(1+v)\chi))(3-3v-6v^2+8(1+v)\chi A) \end{aligned} \quad (48)$$

$$K = \frac{1-v_{23}}{3(1-v)}(3-8(1+v)\chi) \quad (49)$$

where

$$A = 1 + \frac{1}{2}(1-2v)^2 + \frac{(2+v)(1-2v)^2}{(2-v)(1-v)} \quad (50)$$

Equations (46) to (50) are expressions for effective moduli and Poisson's ratio for an axisymmetrically microcracked material, as functions of the original (undamaged) material properties and crack density. In other words, if the elastic properties of an initially homogeneous material and the density of microcracks, which are generated by axial compression are known, the effective moduli and Poisson's ratio in principal directions can be obtained from these equations.

Relationships given in equations (46) through (50) also provide a means of detecting microcrack (damage) density when the effective properties can be measured either statically or dynamically. In Phase II of this research, relationships between dynamic properties and microcrack density will be established and experimentally validated. Non-destructive (ultrasonic, transmitted waves) methodology will be proposed as a means for detecting and quantifying damage (microcrack density) level.

7 Conclusions and Observations

Detailed microstructural alterations (damage) in Indiana limestone and one type of concrete under different loading conditions have been observed using liquid metal alloy preservation techniques. The basic observations/conclusions are as follows:

- As has been cited elsewhere, the basic mechanism for extensile microcracks to initiate in a material under compression is the localized tensile stresses induced by heterogeneities. In Indiana limestone, the mechanisms for the generation of these localized tensile stresses include bending of long grains, point contact between adjacent grains, mismatching elastic properties, boundary discontinuities, pore space and soft inclusion induced tension. In the concrete samples, however, most of the microcracks are generated at grain (aggregate) boundaries.
- Once the microcracks are generated, sometimes at a large inclination angle with respect to the maximum compression, they generally propagate in the direction of the maximum compression. The propagation of these microcracks is controlled initially by the amount of local tensile stress responsible for the generation of the microcracks and the overall confining stress, before any interaction takes place. The generation and propagation of microcracks are speculated to also change the local stress distribution which in turn affects the generation of other microcracks.
- Preliminary statistical results for both the concrete and limestone show that the average length of the microcracks decreases with an increase in confining stress. Average aperture of the microcracks also decreases with an increase in confining stress. The spread of both length and aperture distribution decreases with an increase in confining stress. However, the aspect ratio, the ratio between the aperture of a crack and its length, remains relatively constant for concrete and fluctuates for Indiana limestone. Most of the microcracks are parallel or subparallel to the direction of the maximum compressive stress. The average orientations of microcracks in all of the samples tested are within 15 degrees

deviation from the maximum compressive direction. The density of microcracks, the number of microcracks per unit observed area, increases with an increase in confining stress. This may be due to the higher deviatoric stress which was required to observe any macroscopic alteration of material properties. The relationship between microcrack distribution and stresses applied could not yet be quantified in this phase.

- The macroscopic failure of Indiana limestone samples under unconfined conditions is usually in axial splitting, and under high confining in form of shear bands. The axial splitting of specimens are usually the result of one or several extensile cracks propagating all the way to the ends of the samples. The shear bands are observed to be formed from many short extensile microcracks which are subparallel to the direction of the maximum compression and with their centers slightly offset from each other. The overall effect of these extensile microcracks is a shear band(s) (see Figure 14b).

- Based on the results of a limited number of tests, it was not possible to conclusively determine the relationship between dilatation of samples, microcracks and pore collapse. However, it is speculated that in the post-peak region of stress-strain curves, the volumetric strain of the tested samples is a combination of microcrack dilatation (volume increase) and pore collapse (volume reduction).

- An increase in microcrack density decreases static and dynamic elastic (secant) moduli (qualitatively). This is deduced from continuous measurement of ultrasonic velocities. The relationship between microcrack distribution and stresses applied could be quantified in future effort. "Dynamic" stress-strain curves reconstructed from ultrasonic velocities showed similar behavior to the concurrently generated static stress-strain curves. This suggests that if a relationship between the "dynamic" and static stress-strain curves can be established, non-destructive method such as ultrasonic detection can be used to quantitatively determine and detect the static behavior of a geomaterial and the damage level.

- Theoretical derivations of effective elastic properties of an isotropic material containing axisymmetrically distributed microcracks, using energy conservation principles, showed that moduli of a material decrease with an increase in damage density. This is verified by independent concurrent triaxial compression tests, ultrasonic velocity measurements and microstructural observations. These results show that if a one-to-one relationship can be established between the theoretically derived formulations and microcrack distribution, it could be possible to extrapolate microcrack density at any stage of loading. This requires a calibration of the theoretical formulations given the stress conditions and quantification of microcrack distribution under the same conditions. In a Phase II proposal for this research submitted under separate cover, this calibration and microcrack density extrapolation is proposed.

8 Acknowledgments

Terra Tek, Inc. greatly appreciate Phase I SBIR support provided by AFSOR/XOT for Topic Number AF 90-186, under contract #F49620-90-C-0060.

9 Reference

Ewy, R., Cook, N. G. W. and L. R. Myer, "Hollow cylinder tests for studying fracture around underground openings", Proc. 29th U.S. Symp. Rock Mech., 67-74, Minneapolis, Minnesota, 1989.

Fonseka, G. M., Murrell, S. A. F. and P. Barns, "Scanning electron microscope and acoustic emission studies of crack development in rocks", Int. J. Rock Mech. Min. Sci. & Geomech. Abstr., 273-289, 1985.

Hallbauer, D. K., Wagner, H. and N. G. W. Cook, "Some observations concerning the microscopic and mechanical behavior of quartzite specimens in stiff, triaxial compression tests", Int. J. Rock Mech. Min. Sci., 10, 713-726, 1973.

Pyrak-Nolte, L. J., Myer, L. R., Cook, N. G. W. and P. A. Witherspoon, "Natural fracture in low permeable rock", Proc. 6th Int. Cong. I.S.R.M., 225-231, Montreal, Canada, 1987.

Suarez-Rivera, F. R., Cook, N. G. W., Cooper, G. A. and Z. Zheng, "Indentation by pore collapse in porous rocks", Proc. 31st U.S. Symp. Rock Mech., 671-678, Golden Colorado, 1990.

Wawersik, W. R. and C. A. Fairhurst, "A study of brittle rock failure in laboratory compression experiments," Int. J. Rock Mech. Min. Sci., 7, 561-575, 1970.

Yadev, G. D., Dullien, F. A. L., Chatzis, I. and I. F. Macdonald, "Microscopic distribution of wetting and non-wetting phases in sandstone during immiscible displacements", Paper SPE 13212, Annual Technical Conference and Exhibition, SPE, Dallas, Texas, 1984.

Zheng, Z., Cook, N. G. W. and F. M. Doyle, "A new technique to observe three dimensional cracks in rocks," EOS Trans. AGU, 68, 1477, 1987.

Zheng, Z., Myer, L. R. and N. G. W. Cook, "Microcracks geometry in confined and unconfined conditions," Proc. 30th US Symp. Rock Mech., 749-756, 1989.

APPENDIX A: PERSONNEL

Dr. Ziqiong Zheng
(Principal Investigator)

- Ph.D. Geomechanics, University of California, Berkeley, 1989.
Thesis Title: "Compressive Stress-Induced Microcracks in Rocks and Applications to Seismic Anisotropy and Borehole Stability".
- M.S. Geomechanics, University of California, Berkeley, 1985.
- B.S. Engineering Mechanics and Applied Mathematics, Northeast Institute of Technology, China, 1982.

Dr. John D. McLennan
(Technical Consultant)

- Ph.D. Rock Mechanics, University of Toronto, 1980.
Thesis Title: "Hydraulic Fracturing: A Fracture Mechanics Approach".
- M.A.Sc. Soil Mechanics, University of Toronto, 1976.
Thesis Title: "Study and Analysis of Lateral Pressure in Two Granular Materials".
- B.A.Sc. Geological Engineering, University of Toronto, 1974.

Mr. J. Wesley Martin
(Engineer)

- B.A. Geology (with minor - Physical Science), Humboldt State University, Arcata, California, 1983.
Individual Project: "The study of Microstructures in Quartzites and the Effects of Metamorphism on Quartz Cathodoluminescence using the Scanning Electron Microscope".

APPENDIX B:

Abstract Submitted to the 13th Bi-Annual Logging Symposium of the Canadian Well Logging Society

Dependence of Rock Dynamic Modulus on Stress and Applications

Ziqiong Zheng, John D. McLennan and Wesley J. Martin
Terra Tek, Inc., Salt Lake City, Utah 84108

In-situ stress orientation and magnitude (the principal stress tensor) is important information for designing excavations in rock. For example in petroleum industry, in-situ stresses influence the orientation of deviated wellbores to increase production (by means of stimulation) and to avoid stability problems. When a borehole is drilled, the tangential stress varies angularly, due to stress concentrations caused by removal of the material previously in the borehole. The variation of the stress concentrations is dependent on the far-field (virgin) stress orientations and magnitudes. When the orientations of the near borehole stress concentrations can be determined, it is possible to determine the orientation of the principal stresses. Certain techniques such as micro-hydraulic fracturing, televiwer surveys and mapping of borehole breakouts have been used to deduce magnitudes and/or orientations. Each suffers some specific drawbacks, either requiring prolonged testing in openhole or not providing information which can be definitively used to define the stress state. Elastic wave propagation shows that the velocities of compressional and shear waves travelling through a material depend on the stress state (both axial and confining stresses). In fact, velocity ratios have been used in conjunction with crude assumptions of no lateral deformation to characterize variation in a pseudo-stress field. It is proposed that if the variation of acoustic properties circumferentially around a borehole can be quantified that adaptations of currently existing wireline log interpretation procedures may afford the possibility of determining directionality of stresses and possibly the magnitudes.

Experiments have been performed on rock samples, to assess variation in acoustic characteristics as a function of applied stress magnitude. Cylindrical Indiana limestone samples were oven dried and instrumented to measure deformation as a function of applied stress. After instrumentation, the samples were installed in a pressure vessel and subjected to varying levels of confining pressure. After equilibration, the samples were subjected to triaxial compression at a rate of 10^{-5} in/in/s. Ultrasonic impulses were periodically transmitted through the samples. Compressional and shear wave velocities were measured. From velocity ratios, dynamic mechanical properties (Young's modulus and Poisson's ratio) were calculated and from the variation of these properties with deviatoric stress, artificial "dynamic" stress strain curves were reconstructed. These artificial curves showed similar behavior to static stress-strain curves determined concurrently in the testing. The dynamic modulus of the sample increased with an increase in the applied confining stress and with an increase in the deviatoric axial stress. Near the peak axial stress, dynamic modulus started to decrease, indicating generation of microfractures in the samples. Measuring acoustic velocities at different azimuth, this dependence of dynamic modulus of rock on applied stresses can be used as a means of determining in-situ stress orientation and possibly magnitude.